Page-Curve-Like Dynamics in Integrable Systems

From Quantum Entanglement to Classical Mutual Information

A thesis submitted to the Physics Department of
Indian Institute of Science Education and Research, Pune
in partial fulfillment of the requirements for the
BS–MS Dual Degree Programme

by

Anubhav Mahapatra

Department of Physics
Indian Institute of Science Education and Research, Pune

Supervisors:
Prof. Tridib Sadhu
Associate Professor, DTP, TIFR Mumbai
Prof. Sreejith G.J.
Associate Professor, IISER Pune

भारतीय विज्ञान शिक्षा एवं अनुसंधान संस्थान पुणे
INDIAN INSTITUTE OF SCIENCE EDUCATION AND RESEARCH PUNE
An Autonomous Institution of the Ministry of Education, Govt. of India

Certificate

This is to certify that this dissertation entitled "**Page-Curve-Like Dynamics in Integrable Systems: From Quantum Entanglement to Classical Mutual Information**" towards the partial fulfilment of the BS-MS dual degree programme at the Indian Institute of Science Education and Research, Pune represents study/work carried out by **Anubhav Mahapatra** at Indian Institute of Science Education and Research, Pune under the supervision of Prof. **Tridib Sadhu**, Associate Professor, Department of Theoretical Physics, TIFR Mumbai and Prof. **Sreejith G.J.**, Associate Professor, IISER Pune during the academic year 2025–2026.

Signature of Student	**Signature of Co-Supervisor**	**Signature of Supervisor**

Thesis Advisory Committee:

Prof. Tridib Sadhu (Supervisor)
Prof. Sreejith G.J. (Co-supervisor)
Prof. Bijay Kumar Agarwalla (Expert)

भारतीय विज्ञान शिक्षा एवं अनुसंधान संस्थान पुणे
INDIAN INSTITUTE OF SCIENCE EDUCATION AND RESEARCH PUNE
An Autonomous Institution of the Ministry of Education, Govt. of India

Declaration

I hereby declare that the matter embodied in the report entitled "**Page-Curve-Like Dynamics in Integrable Systems: From Quantum Entanglement to Classical Mutual Information**" are the results of the work carried out by me at the Department of Physics, Indian Institute of Science Education and Research, Pune, under the supervision of Prof. **Tridib Sadhu** and Prof. **Sreejith G.J.** and the same has not been submitted elsewhere for any other degree.

Anubhav Mahapatra		Tridib Sadhu.
Signature of Student	**Signature of Co-Supervisor**	**Signature of Supervisor**

This thesis is based on upcoming research work carried out by the author, his supervisor and co-supervisor.

This thesis is dedicated to everyone who have ever called me by my name.

Statement on Generative AI Usage

I declare that the use of Generative Artificial Intelligence (GAI) in this thesis falls within the scope of Section 4.6.1 of the Guidelines for Generative AI usage at IISER Pune. Accordingly, no attribution is required.

Acknowledgements

I would like to thank my supervisor Prof. Tridib Sadhu for his guidance throughout this work. Interactions with him helped me improve the way I approach physics problems, and the experience of working on this project was an important learning process that strengthened my ability to work independently.

I am grateful to my co-supervisor Prof. Sreejith G.J. for many insightful and engaging discussions that helped shape the direction of this work and provided valuable perspectives during the course of the thesis.

I also thank my expert Prof. Bijay Kumar Agarwalla for his helpful suggestions during the mid-year presentation, which led me to examine several aspects of the project more carefully and ultimately refine the work.

I am deeply grateful to my parents for their constant support and encouragement throughout my studies, and to my friends for helping me navigate the challenges and stresses of this period.

Finally, I acknowledge the IISER Pune community for the experiences and opportunities that shaped my academic journey over the past five years.

Abstract

Entanglement entropy plays an important role in characterizing the buildup of correlations in quantum many-body systems, particularly in non-equilibrium settings. In integrable systems such as free fermions, its dynamical growth can exhibit Page-curve-like behavior and admits an effective large-scale description through generalized hydrodynamics. This raises the question of whether similar entropy dynamics are intrinsically quantum, or whether analogous features can arise in purely classical systems.

In this work, we compare entropy and correlation dynamics in quantum free fermionic systems and the classical hard rod gas. Both systems admit a coarse-grained hydrodynamic description. In the quantum case, the Yang–Yang entropy depends only on quasiparticle mode occupation densities, whereas in the classical hard rod gas the entropy additionally involves the local particle density through an excluded-volume contribution arising from hard-core interactions between rods. While generalized hydrodynamics successfully captures entanglement entropy growth in the quantum case, classical hydrodynamic entropy does not generically reproduce non-monotonic behavior, with its evolution depending on the choice of initial conditions.

To probe correlations beyond hydrodynamic entropy, we compute mutual information in classical hard rod systems, to the extent analytically tractable for this interacting system. Mutual information exhibits non-monotonic behavior—an initial rise followed by decay—with the late-time behavior depending on the system configuration, saturating to a non-zero value in finite systems and decaying to zero in the presence of an infinite reservoir.

These results clarify the extent to which Page-curve-like behavior can emerge in classical systems and highlight the distinct roles played by entropy, correlations, and hydrodynamic descriptions in classical and quantum integrable systems.

Contents

List of Figures

Chapter 1

Introduction

1.1 Entanglement and Non-equilibrium Dynamics

Non-equilibrium dynamics in many-body systems aims to understand how correlations and information evolve with time after a perturbation [1–3]. When an isolated system is driven out of equilibrium, its subsequent evolution results in redistribution of energy, particles and correlations across space. Interactions between particles within the system give rise to nontrivial collective behavior, even without external perturbation. Understanding these correlations is central to condensed matter physics, statistical mechanics and quantum information theory [1, 2].

In quantum systems, correlations between subsystems can be quantified using entanglement entropy [4, 5]. Rather than tracking individual microscopic degrees of freedom, entanglement entropy quantifies the quantum-mechanical correlation between spatial regions. As a system evolves, entanglement typically increases as quasiparticles or excitations propagate and establish correlations between initially disconnected regions. This quasiparticle picture of entanglement spreading was developed by Calabrese and Cardy [3, 6]. This growth of entanglement provides a powerful probe of the underlying dynamical structure [7].

One of the most explored settings is that of a quantum quench, where a system is prepared in an initial state that is not an eigenstate of the Hamiltonian governing its subsequent evolution [1, 3]. After the quench, entanglement entropy often grows linearly at early times in integrable models, reflecting ballistic propagation of quasiparticles [3, 6]. Logarithmic growth is also possible in certain cases such as Luttinger liquid systems [8]. In finite systems or systems coupled to reservoirs, this growth may eventually saturate according to a volume-law scaling of entanglement entropy [2, 7].

In quantum systems such as free fermions or bosons coupled to reservoirs, it has been observed that the entanglement entropy can exhibit non-monotonic behavior and may even decay to zero at long times for particular system-reservoir configurations [9]. This behavior of entropic growth followed by a subsequent decay resembles the so-called Page curve. The Page curve was originally introduced in the context of black hole evaporation to describe the time

evolution of entanglement entropy of Hawking radiation, where the entropy initially increases and eventually decreases back to zero [10, 11].

These observations naturally raise a conceptual question. Entanglement entropy is fundamentally a quantum measure, rooted in the structure of the reduced density matrix and tensor product structure of the Hilbert space. Is the observed rise-and-decay behavior intrinsically tied to quantum entanglement, or does it reflect more general features of correlation transport that might also appear in classical systems? Addressing this question requires a framework that allows a controlled comparison between quantum and classical dynamics at the level of entropy and correlations and their hydrodynamic description.

1.2 Integrable Systems and Generalized Hydrodynamics

A key distinction in non-equilibrium many-body physics is between integrable and non-integrable systems. In general, interacting systems conserve only a few physical quantities like energy and particle number. Therefore, they are expected to thermalize at long time scales. Local observables for non-integrable systems are described by the canonical Gibbs ensemble at large times. This is the essence of the Eigenstate Thermalization Hypothesis (ETH) [12–14].

Integrable systems, in contrast, are characterized by the existence of an extensive set of conserved charges that strongly restrict their dynamics. These additional conservation laws effectively restrict scattering processes and prevent thermalization. Instead, local observables relax to a generalized equilibrium described by a Generalized Gibbs Ensemble (GGE), which incorporates all conserved quantities through corresponding Lagrange multipliers [15, 16]. The GGE density matrix can be written as

$$\rho_{\mathrm{GGE}} \propto \exp\left(-\sum_n \lambda_n Q_n\right) \tag{1.1}$$

λ_n are fixed by the expectation values of the conserved charges Q_n.

GGE is only useful for understanding the stationary properties of the system. To get the full time-dependent evolution of integrable systems we need a coarse-grained, large scale framework. At large macroscopic spacetime scales, we can study the dynamics of the system by a continuum description in terms of local conserved charge densities and currents. For integrable systems, this leads to the framework of generalized hydrodynamics (GHD), which is a natural extension of normal hydrodynamics [17, 18]. The state of the system is described by a local phase-space occupation function which follows the Euler equations governed by quasiparticle velocities.

Generalized Hydrodynamics thus provides a powerful description of entropy and correlation transport in integrable models. Within this framework entropy growth and large time evolution can be analyzed in quantum systems such as free fermions and bosons, which we consider in the following sections.

1.3 Page-Curve-Like Behavior in Quantum Systems

Understanding entanglement entropy gives us great insight into the dynamics of non-equilibrium systems. We divide a system into a region A and its complement $\bar{A}$. Even when the initial state contains little or no entanglement, unitary evolution typically generates correlations between the two regions. The entanglement entropy therefore quantifies how quantum correlations spread across the bipartition as the system evolves.

In integrable systems, this growth can be understood through the quasiparticle picture introduced by Calabrese and Cardy [3,6]. At the time of the quench, the dynamics can be described in terms of quasiparticles, which are stable elementary excitations labeled by a momentum (or rapidity) k and characterized by a dispersion relation ε_k. These quasiparticles are created in pairs with opposite momenta and propagate ballistically through the system with group velocities $v_k = \frac{d\varepsilon_k}{dk}$. At a given time t, only those quasiparticle pairs for which one particle lies inside A while its partner lies in $\bar{A}$ contribute to the entanglement entropy. Their contributions are additive. For a subsystem consisting of an interval of length ℓ, the quasiparticle picture predicts the following expression for the von Neumann entanglement entropy in the scaling limit $t, \ell \to \infty$ with t/ℓ fixed takes the form [19,20]

$$S_A(t) = 2t\int_{2|v_k|t<\ell} \frac{dk}{2\pi}|v_k|s_k + \ell\int_{2|v_k|t\geq\ell} \frac{dk}{2\pi}s_k,$$

where s_k denotes the contribution to the entanglement entropy associated with a quasiparticle pair of momentum k.

This behavior reflects the causal spreading of correlations in many-body systems. If the quasiparticle velocities are bounded by a maximal velocity $v_{\max}$, correlations can only propagate within an effective light-cone region $|x| \leq v_{\max}t$, consistent with the Lieb–Robinson bound [21]. For early times satisfying $2v_{\max}t < \ell$, the second term in the above expression vanishes and the entropy grows linearly in time. This regime corresponds to the continual arrival of entangled quasiparticle pairs across the boundaries of the subsystem. At later times, when $2v_{\max}t \gtrsim \ell$, quasiparticles have traversed the subsystem and the entropy approaches a value that scales with the subsystem size ℓ, consistent with the volume-law.

1.4 Classical Integrable Systems and the Hard Rod Gas

Classical integrable systems provide a natural setting for exploring whether Page-curve-like entropy dynamics can occur without quantum entanglement. Specifically, we can ask if transport of classical correlations can produce similar behavior as that of entropy in quantum systems.

A simple well-known model to probe this is the classical one-dimensional hard rod gas. The system consists of identical rods of mass m and length a, which undergo elastic collisions. The hard rod potential prevents the overlap of these rods, so the separation between the centers

is at least a.

The hard rod gas is an integrable classical system with simple dynamics [22]. During collisions, the rods exchange their velocities, so their velocities remain conserved. Effectively, only the positions of the rods change after a collision. This allows us to map the 1D hard rod gas to a system of ordered point particles with ballistic propagation [23, 24].

In classical systems, correlations are characterized through statistical measures defined on joint probability distributions. This motivates the use of mutual information as a measure of correlations between a system and a reservoir in classical hard-rod systems.

1.5 Mutual Information as a Classical Correlation Measure

Mutual Information is used to quantify correlations between two subsystems in classical statistical systems. For two spatial regions A (system) and B (reservoir), their mutual information $I(A:B)$ measures the statistical dependence between their degrees of freedom. It is based on the joint probability distribution as well as the probability distribution of each region individually. If the configurations of the two regions are completely independent, the joint distribution factorizes and their mutual information vanishes. Therefore, a non-zero mutual information indicates the presence of shared information between the two subsystems. This gives a clear picture about how correlations and number fluctuations are transported across the interface. In this thesis we investigate whether mutual information in classical systems can exhibit Page-curve-like dynamics similar to entanglement entropy in quantum systems. We analyze both the microscopic dynamics and hydrodynamic descriptions for classical particle systems and compare them with known results from quantum systems.

1.6 Scope and Organization of the Thesis

This thesis focuses on the study of correlation dynamics in one-dimensional many-body systems and the comparison between quantum entanglement entropy and classical measures of correlation. Our analysis considers both microscopic descriptions of particle dynamics and coarse-grained hydrodynamic frameworks in order to understand how correlations propagate between a subsystem and a reservoir.

The primary classical model considered in this work is the one-dimensional hard rod gas, an integrable system with ballistic dynamics and a well-defined hydrodynamic description. Correlations between the system and reservoir are quantified using mutual information, which allows us to study the transport and growth of classical correlations. In addition to the hard rod model, we also examine diffusive dynamics of Brownian particles across a semi-permeable interface as a complementary setting for understanding correlation transport.

The remainder of the thesis is organized as follows. Chapter 2 introduces the quantum

fermionic model and reviews the calculation of entanglement entropy together with its hydrodynamic description. Chapter 3 presents the classical hard rod model and derives the corresponding entropy functional within a hydrodynamic framework. Chapter 4 develops the formulation of mutual information for classical particle systems and discusses both ballistic and diffusive dynamics. Chapter 5 discusses the comparisons between microscopic calculations and hydrodynamic predictions. Finally, Chapter 6 summarizes the main results and discusses possible extensions and future directions of this work.

Chapter 2

Quantum Free Fermions: Microscopic and Hydrodynamic Description

This chapter is largely based on work done in [9]. The chapter is devoted to the study of a free fermionic chain defined on a uniformly spaced lattice, where a finite system is coupled to a large reservoir through a local defect Free fermionic models allow for an exact treatment of non-equilibrium dynamics because their quadratic Hamiltonian can be described precisely in terms of single-particle modes.

Initially, all fermions occupy the finite subsystem while the reservoir is empty. Once the coupling between the two regions is switched on, particles propagate across the junction and correlations build up between the system and the reservoir. The resulting dynamics provides a natural setting to study the evolution of entanglement and particle transport in an integrable quantum system.

The microscopic dynamics can be analyzed exactly using the correlation matrix formalism, while GHD provides a complementary coarse-grained description in terms of quasiparticle transport. In this chapter we review the model and the scattering properties of the defect, then review the correlation matrix approach used to compute the von Neumann (entanglement) entropy, and finally present the hydrodynamic description of the system. The free fermion model serves as a useful reference case whose exact solution provides insight into the corresponding hydrodynamic behavior that will later be compared with classical particle systems.

2.1 Model and Quench Setup

We consider a one-dimensional lattice of spinless fermions occupying sites labeled by integers n. The fermionic creation and annihilation operators at site n are denoted by $\hat{c}_n^\dagger$ and $\hat{c}_n$, respectively. The system consists of a finite segment coupled to a much larger reservoir through a local defect.

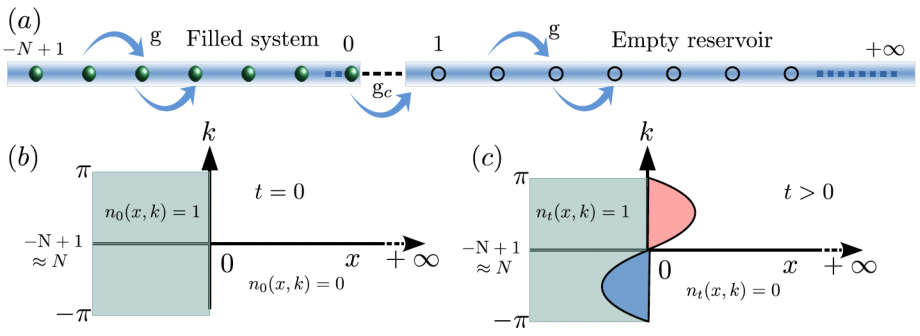

Figure 2.1: A schematic of the free fermion system

The lattice extends from $n = -N+1$ to $n = N_b$, where $N_b \gg N$. The sites $n \leq 0$ form the finite subsystem, while the sites $n \geq 1$ constitute the reservoir. Initially the subsystem is completely filled with fermions and the reservoir is empty. At time $t = 0$, the two regions are coupled through a local defect at the junction, after which the system evolves unitarily.

The dynamics are governed by a nearest-neighbour tight-binding Hamiltonian of the form

$$\hat{H} = \sum_{i,j=-N+1}^{N_b} h_{ij}, \hat{c}_i^\dagger \hat{c}_j, \tag{2.1}$$

where the matrix elements h_{ij} describe the hopping amplitudes. Away from the junction the lattice is homogeneous, with

$$h_{ij} = -g(\delta_{i,j+1} + \delta_{i+1,j}), \tag{2.2}$$

where g denotes the nearest-neighbour hopping strength. The corresponding single-particle dispersion relation of the homogeneous chain is

$$E(k) = -2g\cos k. \tag{2.3}$$

At the boundary between the subsystem ($-N+1 \leq i, j \leq 0$) and the reservoir ($1 \leq i, j \leq N_b$), the coupling is modified by a local defect. The precise form of this defect determines the scattering properties at the junction, which will be discussed in the next section.

2.2 Local Defects and Scattering Theory

The coupling between the subsystem and the reservoir occurs through a local defect at the junction between sites $n = 0$ and $n = 1$. This defect breaks the translational invariance of the homogeneous tight-binding chain and introduces scattering of single-particle excitations.

In the thermodynamic limit ($N \to \infty$), the dynamics near the junction can be understood in terms of a single-particle scattering problem. An incoming plane wave from the left is partially transmitted into the reservoir and partially reflected back into the subsystem. The scattering

properties of the junction are characterized by the reflection and transmission probabilities, denoted by R_k and T_k, respectively [25].

In this work we consider three types of local defects, which differ in how the coupling matrix elements h_{ij} are modified at the junction. The resulting scattering coefficients determine how quasiparticles propagate between the subsystem and the reservoir.

2.2.1 Conformal Defect

The conformal defect is a finely tuned junction designed such that the reflection and transmission probabilities are independent of momentum. This property is associated with scale invariance in the low-energy limit.

The defect modifies both the hopping amplitude across the junction and the on-site potentials at the two sites adjacent to it:

$$h_{0,1} = h_{1,0} = -g_c, \qquad h_{0,0} = -h_{1,1} = \sqrt{g^2 - g_c^2}. \tag{2.4}$$

Introducing the dimensionless parameter

$$\lambda = \frac{g_c}{g}, \tag{2.5}$$

the resulting scattering probabilities are

$$T_k = \lambda^2, \qquad R_k = 1 - \lambda^2. \tag{2.6}$$

Notably, both probabilities are independent of the wave vector k. This momentum-independent transmission is a defining property of conformal defects and reflects the scale-invariant structure of the junction.

2.2.2 Hopping Defect

In the hopping defect, only the hopping amplitude across the junction is modified while the on-site potentials remain unchanged:

$$h_{0,1} = h_{1,0} = -g_c, \qquad h_{0,0} = h_{1,1} = 0. \tag{2.7}$$

This configuration models a weak link or tunneling barrier between the subsystem and the reservoir. In contrast to the conformal defect, the scattering coefficients now depend on the momentum of the incoming particle.

The reflection probability takes the form

$$R_k = \frac{(\lambda^2-1)^2}{\lambda^4+1-2\lambda^2\cos(2k)}, \tag{2.8}$$

with transmission probability

$$T_k = 1 - R_k. \tag{2.9}$$

2.2.3 Density Defect

The density defect corresponds to a localized potential perturbation at the junction. In this case the hopping amplitude remains unchanged while the on-site potentials at the junction sites are modified:

$$h_{0,0} = h_{1,1} = g_c, \qquad h_{0,1} = h_{1,0} = -g. \tag{2.10}$$

Such a defect can be interpreted as a local potential barrier or well. The resulting reflection probability is given by

$$R_k = \frac{\lambda^2(\lambda-2\cos k)^2}{2+2\lambda^2+\lambda^4-4\lambda^3\cos k+2(\lambda^2-1)\cos(2k)}, \tag{2.11}$$

with

$$T_k = 1 - R_k. \tag{2.12}$$

2.2.4 Scattering Ansatz

The reflection and transmission coefficients are obtained by solving the single-particle scattering problem at the junction. We consider an incoming plane wave from the subsystem side with wave vector k. The stationary wavefunction takes the form

$$\psi_n = \begin{cases} e^{ikn} + r_k e^{-ikn}, & n \leq 0, \\ t_k e^{ikn}, & n \geq 1, \end{cases} \tag{2.13}$$

where r_k and t_k denote the reflection and transmission amplitudes. The corresponding energy follows from the dispersion relation of the homogeneous chain,

$$E = -2g\cos k. \tag{2.14}$$

Substituting this ansatz into the time-independent Schrödinger equation at the defect sites yields a set of linear equations for r_k and t_k. Solving these equations leads to the expressions for $R_k = |r_k|^2$ and $T_k = |t_k|^2$ given above. The detailed derivation for each type of defect is presented in Appendix A.

2.3 Correlation Matrix Formalism

The microscopic dynamics of the free fermionic system can be computed exactly using the correlation matrix formalism. Since the Hamiltonian is quadratic in fermionic operators, the many-body state remains Gaussian during the time evolution. As a consequence, all physical observables can be expressed in terms of the two-point correlation functions.

2.3.1 Quadratic Fermionic Hamiltonian

We consider a finite-dimensional, non-interacting fermionic system described by the quadratic Hamiltonian [9]

$$\hat{H} = \sum_{i,j=-N+1}^{N_b} h_{ij}\, \hat{c}_i^\dagger \hat{c}_j, \tag{2.15}$$

where $\hat{c}_i^\dagger$ and $\hat{c}_i$ are fermionic creation and annihilation operators at lattice site i, and h_{ij} are the single-particle hopping matrix elements of the tight-binding Hamiltonian.

It is convenient to introduce the column vector of annihilation operators

$$D = \begin{pmatrix} \hat{c}_{-N+1} \\ \hat{c}_{-N+2} \\ \vdots \\ \hat{c}_{N_b} \end{pmatrix}, \qquad D^\dagger = \begin{pmatrix} \hat{c}^\dagger_{-N+1} & \hat{c}^\dagger_{-N+2} & \cdots & \hat{c}^\dagger_{N_b} \end{pmatrix}. \tag{2.16}$$

In this notation the Hamiltonian can be written in compact matrix form as

$$\hat{H} = D^\dagger h D, \tag{2.17}$$

where h is the single-particle tight-binding Hamiltonian matrix.

2.3.2 Heisenberg Time Evolution

The time evolution of the fermionic operators follows from the Heisenberg equation of motion,

$$\frac{d\hat{c}_j(t)}{dt} = -i \sum_n h_{jn}\, \hat{c}_n(t). \tag{2.18}$$

In vector form this becomes

$$\frac{dD(t)}{dt} = -i h D(t). \tag{2.19}$$

The formal solution is therefore

$$D(t) = e^{-iht} D(0), \qquad D^\dagger(t) = D^\dagger(0) e^{iht}. \tag{2.20}$$

2.3.3 Correlation Matrix

The equal-time correlation matrix is defined as

$$C_{ij}(t) = \langle \hat{c}_i^\dagger(t)\hat{c}_j(t)\rangle. \tag{2.21}$$

Using the operator evolution above, the correlation matrix evolves according to the similarity transformation

$$C(t) = e^{iht}C(0)e^{-iht}. \tag{2.22}$$

This relation allows the exact computation of the microscopic dynamics of the system.

2.3.4 Initial State

In the quench protocol considered here, the finite subsystem (sites $-N+1$ to 0) is initially completely filled with fermions, while the reservoir (sites 1 to N_b) is empty. The initial correlation matrix therefore takes the form

$$C_{ij}(0) = \begin{cases} \delta_{ij}, & i,j \in [-N+1,0], \\ 0, & \text{otherwise.} \end{cases} \tag{2.23}$$

2.3.5 Observables from the Correlation Matrix

Once $C(t)$ has been computed, physical observables can be obtained directly from its matrix elements.

The local particle density at site i is given by

$$\rho(i,t) = \langle \hat{c}_i^\dagger(t)\hat{c}_i(t)\rangle = C_{ii}(t). \tag{2.24}$$

Similarly, the particle current across the junction between sites 0 and 1 can be written as

$$I(t) = 2g_c \,\mathrm{Im}\Big[\langle \hat{c}_0^\dagger(t)\hat{c}_1(t)\rangle\Big] = 2g_c \,\mathrm{Im}[C_{01}(t)]. \tag{2.25}$$

The derivation of the current operator from the Heisenberg equation of motion is provided in Appendix C.

2.4 Entanglement Entropy from Mode Occupations

The entanglement between the finite subsystem and the reservoir can be computed directly from the correlation matrix [26]. Since the Hamiltonian is quadratic in fermionic operators, the many-body state remains Gaussian during the time evolution. A key consequence of this

property is that the reduced density matrix of any subsystem is completely determined by its two-point correlation functions.

To quantify the entanglement between the subsystem and the reservoir, we restrict the full correlation matrix $C(t)$ to the subsystem sites. Let

$$A = \{-N+1, \ldots, 0\} \tag{2.26}$$

denote the set of subsystem sites. The subsystem correlation matrix is defined as

$$C_A(t) = \big[C_{ij}(t)\big]_{i,j\in A}. \tag{2.27}$$

Since $C_A(t)$ is Hermitian, it admits a unitary diagonalization

$$C_A(t) = U^\dagger \Lambda U, \tag{2.28}$$

where

$$\Lambda = \mathrm{diag}(m_1, m_2, \ldots, m_N) \tag{2.29}$$

contains the eigenvalues of the subsystem correlation matrix. These eigenvalues satisfy

$$0 \leq m_\ell \leq 1, \tag{2.30}$$

and can be interpreted as occupation probabilities of a set of single-particle *entanglement modes*.

The unitary matrix U defines new fermionic operators

$$\hat{a}_\ell = \sum_{i\in A} U_{\ell i}\hat{c}_i, \tag{2.31}$$

which diagonalize the subsystem correlation matrix,

$$\langle \hat{a}_\ell^\dagger \hat{a}_{\ell'} \rangle = m_\ell \delta_{\ell\ell'}. \tag{2.32}$$

For Gaussian fermionic states the reduced density matrix of the subsystem can be written as the exponential of a quadratic operator, often referred to as the *entanglement Hamiltonian*. In the basis that diagonalizes the correlation matrix, the reduced density matrix factorizes into independent fermionic modes. Each mode behaves as an effective two-level system with occupation probability m_ℓ.

As a consequence, the von Neumann entropy of the subsystem can be expressed entirely in terms of the eigenvalues of the correlation matrix,

$$S(t) = -\sum_{\ell=1}^{N} \left[m_\ell \ln m_\ell + (1-m_\ell)\ln(1-m_\ell)\right]. \tag{2.33}$$

Thus, the entanglement entropy is completely determined by the single-particle eigenvalues of the subsystem correlation matrix. A detailed derivation of this relation is provided in Appendix B.

2.5 Hydrodynamic Description and Yang–Yang Entropy

The microscopic description presented in the previous sections allows the exact computation of observables using the correlation matrix. However, at large spatial and temporal scales it is often more convenient to use a coarse-grained description of the dynamics. For integrable systems this is provided by the framework of generalized hydrodynamics (GHD) [17, 18], which describes the evolution of the system in terms of semiclassical quasiparticles.

2.5.1 Quasiparticle Picture

In integrable systems the elementary excitations behave as stable quasiparticles labeled by their momentum k. Instead of tracking the microscopic fermionic operators, GHD describes the system through a coarse-grained phase-space occupation density

$$n_t(x,k) \in [0,1], \tag{2.34}$$

which represents the local occupation probability of quasiparticles with momentum k around position x at time t.

This function can be interpreted as the hydrodynamic analogue of the microscopic correlation matrix, providing a coarse-grained description of particle occupations in both position and momentum space.

2.5.2 Free Fermionic Case

For the tight-binding Hamiltonian introduced in Section 2.1, the single-particle dispersion relation is

$$E(k) = -2g\cos k. \tag{2.35}$$

The corresponding quasiparticle group velocity is

$$v_k = \frac{\partial E(k)}{\partial k} = 2g\sin k. \tag{2.36}$$

In the bulk of the system the quasiparticles propagate ballistically with velocity v_k. At the defect located at $x = 0$, however, they can be partially reflected or transmitted according to the reflection and transmission probabilities R_k and T_k derived in Section 2.2.

2.5.3 Euler Hydrodynamic Equation

The evolution of the quasiparticle occupation function follows from the conservation of particles in phase space. For free fermions the momentum k is conserved during the motion, and the occupation density obeys the Euler-scale transport equation [9]

$$\partial_t n_t(x,k) + v_k \, \partial_x n_t(x,k) = 0, \qquad v_k = 2g \sin k. \tag{2.37}$$

This equation simply expresses that quasiparticles propagate ballistically along trajectories with constant momentum and velocity v_k.

The solution of this equation is obtained by transporting the initial occupation profile along the quasiparticle trajectories,

$$n_t(x,k) = n_0(x - v_k t, k), \tag{2.38}$$

subject to the boundary conditions imposed by the reflecting wall at $x = -N$ and the partially transmitting defect at $x = 0$ and

$$n_0(x,k) = \theta(-x) - \theta(-x-N)$$

Once $n_t(x,k)$ is known, hydrodynamic observables can be obtained by integrating over momentum. For instance, the particle density is

$$\rho(x,t) = \int_{-\pi}^{\pi} \frac{dk}{2\pi} n_t(x,k), \tag{2.39}$$

and the total number of particles in the subsystem is

$$N(t) = \int_{-N}^{0} dx \, \rho(x,t). \tag{2.40}$$

2.5.4 Yang–Yang Entropy

Within the hydrodynamic framework the entropy associated with the local quasiparticle distribution is given by the *Yang–Yang entropy*. This entropy was originally derived by Yang and Yang in their thermodynamic Bethe ansatz description of one-dimensional integrable systems [27]. In that context, the entropy arises from counting the number of microscopic configurations corresponding to a given distribution of quasiparticles and holes in rapidity space.

In the hydrodynamic description this information is encoded in the local occupation function $n_t(x,k)$, which represents the probability that a quasiparticle state with momentum k near position x is occupied. The Yang–Yang entropy therefore measures the number of ways of arranging occupied and unoccupied quasiparticle states.

For fermionic quasiparticles it takes the form [9]

$$s_{\mathrm{hydro}}(x,t) = -\int_{-\pi}^{\pi} \frac{dk}{2\pi} \Big[n_t(x,k) \ln n_t(x,k) + (1-n_t(x,k)) \ln(1-n_t(x,k)) \Big]. \tag{2.41}$$

We define the entropy of the subsystem and of the reservoir as

$$S^{(S)}_{\mathrm{hydro}}(t) = \int_{-N}^{0} dx\, s_{\mathrm{hydro}}(x,t), \qquad S^{(R)}_{\mathrm{hydro}}(t) = \int_{0}^{N_b} dx\, s_{\mathrm{hydro}}(x,t). \tag{2.42}$$

Physically, this entropy measures the local combinatorial freedom of arranging particles and holes among the available quasiparticle states. In particular, a configuration with $n_t = 0$ or $n_t = 1$ corresponds to a fully empty or fully occupied set of states and therefore carries zero entropy.

This expression has the same functional form as the entropy obtained from the microscopic correlation matrix in Section 2.4. In that case the entropy was expressed in terms of the eigenvalues m_ℓ of the subsystem correlation matrix,

$$S(t) = -\sum_{\ell} \big[m_\ell \ln m_\ell + (1-m_\ell) \ln(1-m_\ell) \big]. \tag{2.43}$$

In the hydrodynamic description the function $n_t(x,k)$ plays an analogous role to the microscopic occupation numbers m_ℓ. The Yang–Yang entropy therefore represents the coarse-grained, hydrodynamic counterpart of the microscopic entanglement entropy.

2.6 Comparison Between Microscopic and Hydrodynamic Results

In this section we compare the exact microscopic results obtained from the correlation matrix formalism with the predictions of the hydrodynamic description introduced in the previous section. The comparison is performed for three types of defects: conformal, hopping, and density defects.

We analyze three observables: the particle density profile, the current across the junction, and the entanglement entropy. The microscopic quantities are computed numerically from the correlation matrix, while their hydrodynamic counterparts are obtained from the occupation function $n_t(x,k)$.

The numerical simulations are performed for a finite subsystem of size $N = 80$ coupled to a reservoir of size $N_b = 4096$, with hopping amplitude $g = 0.5$. The defect strength is parameterized by $\lambda = g_c/g = 0.8$. The time evolution of the correlation matrix is computed numerically, and observables are extracted from $C(t)$ as described in the previous sections. Hydrodynamic predictions are obtained from the coarse-grained occupation function $n_t(x,k)$.

2.6.1 Density Profiles

We first compare the spatial density profiles predicted by the microscopic dynamics and by generalized hydrodynamics.

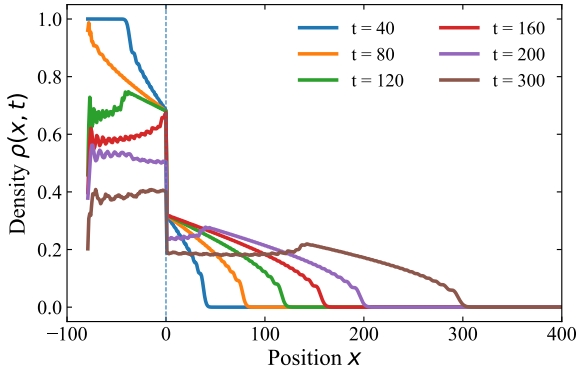

(a) Exact numerical density

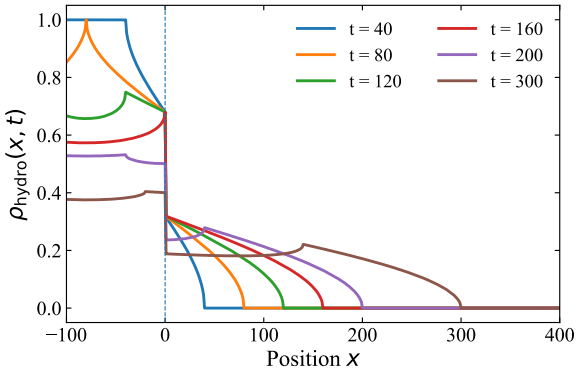

(b) Hydrodynamic prediction

Figure 2.2: Density profiles for the conformal defect

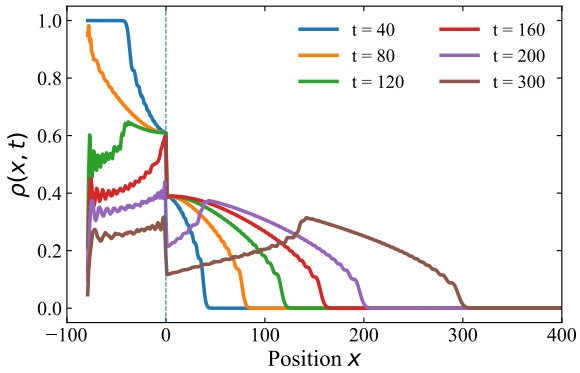

(a) Exact numerical density

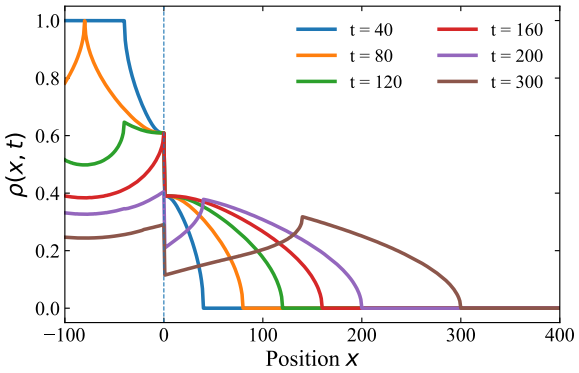

(b) Hydrodynamic prediction

Figure 2.3: Density profiles for the hopping defect

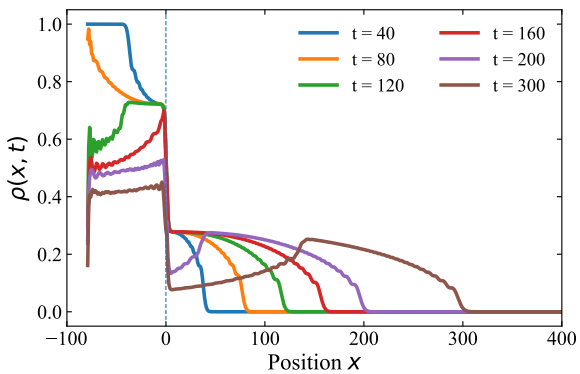

(a) Exact numerical density

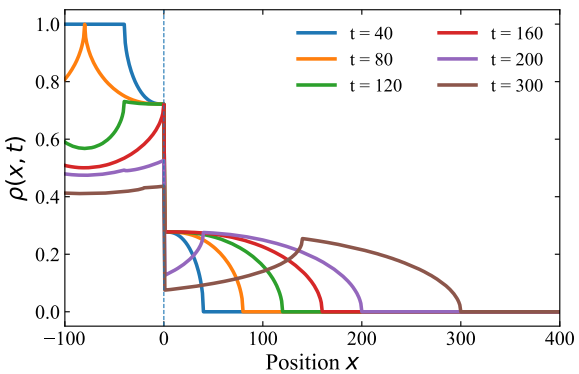

(b) Hydrodynamic prediction

Figure 2.4: Density profiles for the density defect

The hydrodynamic description captures the overall evolution of the density profile remarkably well. In particular, the ballistic propagation of the density fronts and their broad spatial structure are reproduced accurately for all three types of defects.

The microscopic results exhibit additional oscillatory structures that are absent in the hydrodynamic prediction. These oscillations originate from coherent single-particle interference effects and are therefore intrinsically microscopic. Since generalized hydrodynamics describes the system only at the Euler (coarse-grained) scale, such oscillations are averaged out in the hydrodynamic description.

Slight deviations are also observed near the reflecting wall at $x = -N$, where additional reflections produce interference effects that are not captured within the coarse-grained hydrodynamic framework.

2.6.2 Power-law decay of the entropy

At late times the entropy exhibits a clear power-law decay. To analyze this behavior more clearly we examine the entropy on a log-log scale.

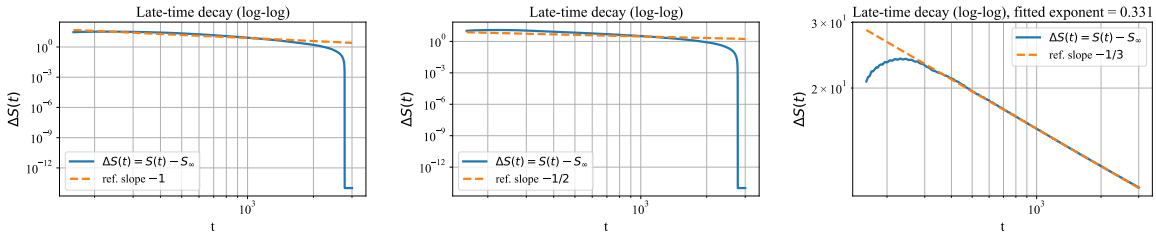

Figure 2.5: Log-log plots of the late-time entropy decay for the three defects

From the slopes of these curves we observe approximate decay exponents

$$S(t) \sim t^{-1}, \quad t^{-1/2}, \quad t^{-1/3}, \tag{2.44}$$

for the conformal, hopping, and density defects respectively, which was also shown in [9].

These distinct exponents reflect the different scattering properties of the defects and the resulting large-time asymptotics of the quasiparticle phase-space distribution. The appearance of clear power-law behavior further supports the hydrodynamic picture of entropy dynamics at long times.

2.6.3 Entanglement Entropy

Finally, we examine the time evolution of the entanglement entropy of the subsystem.

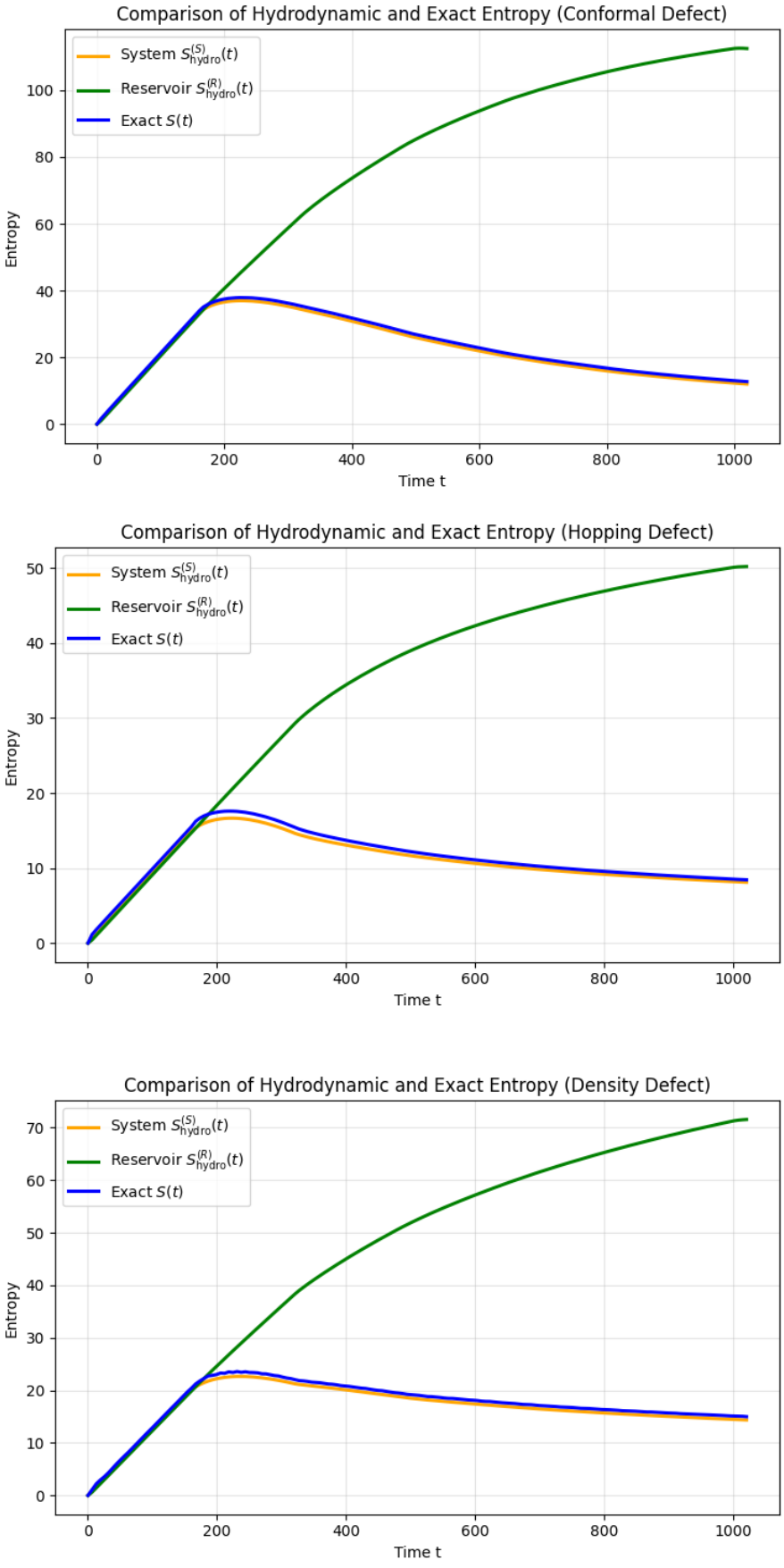

Figure 2.6: Comparison of the exact microscopic entropy and the hydrodynamic prediction for the conformal, hopping, and density defects

For all three defects the entropy initially grows linearly in time, reflecting the steady flow of quasiparticles across the junction. This growth continues until the so-called *Page time*, after which the entropy begins to decrease as the subsystem progressively empties. The Page time corresponds approximately to the time at which the quasiparticle front reaches the boundary of the subsystem.

Overall, the hydrodynamic entropy provides an accurate coarse-grained description of the microscopic entanglement dynamics.

2.7 Summary

The results presented in this chapter reproduce the main findings of [9], who studied the dynamics of a finite fermionic subsystem coupled to a reservoir through a defect using both microscopic and hydrodynamic methods. Reproducing these results serves as an important benchmark for the present work and allows us to verify the numerical implementation of the correlation matrix dynamics and its hydrodynamic description.

Having established this correspondence for the quantum free-fermion system, we next investigate whether similar hydrodynamic structures emerge in classical particle systems. In the following chapter we study the dynamics of classical hard rods and explore the connection between hydrodynamic entropy and classical mutual information.

Chapter 3

Classical Hard Rod Gas: Microscopic Model and Hydrodynamics

In the previous chapter, we studied the non-equilibrium dynamics of a quantum free-fermion system and showed that the hydrodynamic description accurately reproduces the evolution of the entanglement entropy of a subsystem coupled to a reservoir. This naturally raises the question of whether similar hydrodynamic entropy structures can appear in purely classical particle systems.

In this chapter, we investigate the dynamics of a one-dimensional gas of classical hard rods. We first introduce the microscopic hard-rod model and derive the associated entropy functional, and then analyze the hydrodynamic evolution of this entropy for a system coupled to a reservoir. Both the quantum and classical cases share the same coarse-grained structure: entropy counts the number of microscopic configurations compatible with a given coarse-grained distribution. In the quantum case these are occupation configurations of single-particle modes; here they are phase-space configurations of rods consistent with the distribution $f(x,t,v)$

3.1 Microscopic Hard Rod Dynamics

We consider a one-dimensional classical gas of M identical hard rods of length $a > 0$ [22, 28]. Each rod is characterized by a position $q_j(t)$ and velocity $p_j(t)$, with $j = 1,\ldots,M$. For convenience, we set the mass of each rod to unity so that the velocity and momentum coincide. We use M instead of N as we use N for boundary conditions.

The hard-core constraint prevents rods from overlapping, and the coordinates therefore satisfy the ordering condition

$$q_{j+1}(t) - q_j(t) \geq a, \qquad j = 1,\ldots,M-1. \tag{3.1}$$

Between collisions, the rods move ballistically with constant velocity.

$$\dot{q}_j(t) = p_j. \tag{3.2}$$

When two rods collide their velocities are exchanged. Equivalently, one may label the particles such that the velocities remain attached to the same labels while the particle coordinates undergo jumps of size $\pm a$ at collision events. In this representation particle trajectories are piecewise linear, with discontinuous shifts of the positions arising from the hard-core interaction.

It is convenient to introduce the microscopic phase-space density [29]

$$\mathbf{n}(x,t,v) = \sum_{j=1}^{M} \delta(x - q_j(t))\, \delta(v - p_j). \tag{3.3}$$

The quantity

$$\mathbf{n}(x,t,v)\, dx\, dv$$

represents the number of rods whose positions lie in the interval $[x, x+dx]$ and whose velocities lie in $[v, v+dv]$. Because velocities are conserved in collisions (up to exchange of particle labels), the velocity v acts as a conserved label in the hydrodynamic description.

The microscopic density satisfies the local conservation law

$$\partial_t \mathbf{n}(x,t,v) + \partial_x j(x,t,v) = 0, \tag{3.4}$$

where $j(x,t,v)$ denotes the corresponding current density.

At the hydrodynamic (Euler) scale it is convenient to work with a coarse-grained phase-space distribution obtained by averaging the microscopic field over mesoscopic space-time cells. We define

$$f(x,t,v) = \langle \mathbf{n}(x,t,v) \rangle, \tag{3.5}$$

where $\langle \cdot \rangle$ denotes the average with respect to the local generalized Gibbs ensemble (GGE) [29]. Physically, $f(x,t,v)$ is obtained by averaging $\mathbf{n}$ over a mesoscopic region around (x,t), large enough to contain many particles but small compared to the scale of macroscopic variation.

Macroscopic observables can be obtained by integrating the distribution over velocities. In particular the particle density and current are

$$\rho(x,t) = \int_{\mathbb{R}} dv\, f(x,t,v), \qquad j(x,t) = \int_{\mathbb{R}} dv\, v\, f(x,t,v). \tag{3.6}$$

Due to the finite size of the rods, interactions affect the propagation of particles through repeated collisions. While individual collisions simply exchange velocities, their cumulative effect leads to a systematic renormalization of particle trajectories at the coarse-grained level.

In the hydrodynamic description, the rods thus act as quasiparticles whose propagation is

dressed by excluded-volume interactions. It is therefore natural to introduce an effective velocity $v_{\text{eff}}(v)$, defined as the velocity at which quasiparticles with bare velocity v are transported in the interacting medium.

For the hard-rod gas, the effective velocity is given by [28, 29]

$$v_{\text{eff}}(v) = \frac{v - a\rho u}{1 - a\rho}, \tag{3.7}$$

where

$$u = \frac{1}{\rho} \int dv\, v f(x,t,v) \tag{3.8}$$

is the local mean velocity. The denominator $1 - a\rho$ represents the fraction of available free space due to the excluded volume of the rods. The numerator $v - a\rho u$ captures the net shift in particle trajectories induced by collisions with surrounding rods. Together, these contributions determine the effective propagation velocity of quasiparticles in the interacting medium.

The fields introduced above provide the basic hydrodynamic description of the hard-rod gas. In the following section we derive the corresponding entropy functional associated with the coarse-grained phase-space distribution $f(x,t,v)$.

3.2 Derivation of the Hard-Rod Entropy Functional

We now derive the entropy functional associated with the coarse-grained phase-space distribution $f(x,t,v)$ introduced in the previous section. Such entropy functionals for integrable systems have been previously obtained within hydrodynamic and fluctuation frameworks [30].

3.2.1 Mesoscopic phase-space description

Consider a mesoscopic spatial cell

$$I = [x, x + \Delta x],$$

where Δx is large compared to microscopic scales ($\Delta x >> a$) so that the cell contains many rods but small on macroscopic hydrodynamic scales. We partition velocity space into bins

$$B_\alpha = [v_\alpha, v_\alpha + \Delta v], \qquad \alpha = 1, 2, \ldots, M.$$

The occupation number of bin α is defined as

$$N_\alpha := \int_I dx' \int_{B_\alpha} dv'\, \mathbf{n}(x', v'; t). \tag{3.9}$$

A local macrostate specified by the hydrodynamic distribution $f(x,t,v)$ corresponds to fixing the velocity histogram

$$N_\alpha \simeq f(x,t,v_\alpha)\, \Delta x \Delta v, \qquad \forall\, \alpha. \tag{3.10}$$

The total number of rods in the cell is therefore

$$N_{\text{cell}} := \sum_{\alpha} N_{\alpha} \simeq \Delta x \int_{\mathbb{R}} dv\, f(x,t,v) = \rho(x,t)\Delta x. \tag{3.11}$$

3.2.2 Local entropy density

The entropy density is defined as the entropy per unit length associated with the mesoscopic cell I,

$$s(x,t) = k_B \lim_{\Delta x \to 0} \frac{1}{\Delta x} \log \Omega(I;\{N_\alpha\}), \tag{3.12}$$

where $\Omega(I;\{N_\alpha\})$ denotes the number of microscopic configurations compatible with the constraints described earlier. The limit $\Delta x \to 0$ is understood in the hydrodynamic sense: Δx is taken to be small compared to macroscopic variation length scales while remaining large compared to microscopic scales such as the rod length a, so that the cell contains many rods and local thermodynamic descriptions apply.

3.2.3 Counting microscopic configurations

Since velocities are conserved in collisions and the hard-core constraint affects only spatial configurations, the counting of microstates factorizes into independent velocity and configurational contributions.

Velocity assignment multiplicity The number of ways to assign velocities to the rods such that exactly N_α rods lie in bin B_α is multinomial,

$$\Omega_{\text{vel}}(\{N_\alpha\}) = \frac{N_{\text{cell}}!}{\prod_\alpha N_\alpha!}. \tag{3.13}$$

Configurational volume. For N_{cell} rods in a segment of length Δx, the available configurational phase-space volume [24] is

$$\Omega_{\text{conf}}(N_{\text{cell}},\Delta x) = \frac{1}{N_{\text{cell}}!} \prod_{j=1}^{N_{\text{cell}}} (\Delta x - ja). \tag{3.14}$$

Total number of microstates Combining the two contributions gives

$$\Omega(I;\{N_\alpha\}) = \Omega_{\text{vel}}(\{N_\alpha\})\,\Omega_{\text{conf}}(N_{\text{cell}},\Delta x) = \frac{1}{\prod_\alpha N_\alpha!} \prod_{j=1}^{N_{\text{cell}}} (\Delta x - ja). \tag{3.15}$$

Hence

$$\log \Omega(I;\{N_\alpha\}) = -\sum_\alpha \log N_\alpha! + \sum_{j=1}^{N_{\text{cell}}} \log(\Delta x - ja). \tag{3.16}$$

3.2.4 Velocity contribution

Using Stirling's approximation $\log m! \simeq m\log m - m$,

$$\log N_\alpha! \simeq N_\alpha \log N_\alpha - N_\alpha.$$

Substituting $N_\alpha \simeq f(x,t,v_\alpha)\Delta x \Delta v$ yields

$$-\frac{1}{\Delta x}\sum_\alpha \log N_\alpha! = -\int_{\mathbb{R}} dv\, f(x,t,v)\log f(x,t,v) - \rho(x,t)\log(\Delta x \Delta v) + \rho(x,t) + \text{const.} \quad (3.17)$$

The first term represents the usual mixing entropy associated with the velocity distribution. Here and in the following, the constant term denotes terms independent of the local distribution $f(x,t,v)$ and therefore irrelevant for the hydrodynamic entropy.

3.2.5 Configurational contribution

Rewrite

$$\log(\Delta x - ja) = \log \Delta x + \log\Big(1 - \frac{aj}{\Delta x}\Big).$$

Then

$$\sum_{j=1}^{N_{\text{cell}}} \log(\Delta x - ja) = N_{\text{cell}} \log \Delta x + \sum_{j=1}^{N_{\text{cell}}} \log\Big(1 - \frac{aj}{\Delta x}\Big). \quad (3.18)$$

Introducing $\rho = N_{\text{cell}}/\Delta x$ and approximating the sum by an integral,

$$y = \frac{aj}{\Delta x}, \qquad dy = \frac{a}{\Delta x} dj,$$

gives

$$\frac{1}{\Delta x}\sum_{j=1}^{N_{\text{cell}}} \log\Big(1 - \frac{aj}{\Delta x}\Big) = \frac{1}{a}\int_0^{a\rho} \log(1-y)\, dy. \quad (3.19)$$

Evaluating the integral,

$$\int_0^{a\rho} \log(1-y)\, dy = -(1-a\rho)\log(1-a\rho) - a\rho,$$

we obtain

$$\frac{1}{\Delta x}\sum_{j=1}^{N_{\text{cell}}} \log(\Delta x - ja) = \rho \log \Delta x - \Big(\frac{1}{a} - \rho\Big)\log(1-a\rho) - \rho + \text{const.} \quad (3.20)$$

3.2.6 Entropy functional

Combining (3.17) and (3.20), the terms $\pm\rho$ cancel and the dependence on $\rho \log \Delta x$ cancels between the velocity and configurational contributions. The entropy density therefore takes the

form [29]

$$s(x,t) = -k_B \int_{\mathbb{R}} dv\, f(x,t,v) \log f(x,t,v) - k_B \Big(\frac{1}{a} - \rho(x,t)\Big) \log(1 - a\rho(x,t)) + \text{const.} \quad (3.21)$$

Here $\rho(x,t) = \int dv\, f(x,t,v)$. The remaining term proportional to $\rho \log \Delta v$ depends only on the choice of velocity discretization and not on the functional form of $f(x,t,v)$. It therefore contributes an additive constant to the entropy density and can be omitted, as only variations of the entropy functional are physically relevant. We next proceed to the point hard-rod limit.

3.3 Point-Particle Limit ($a \to 0$)

The hard-rod entropy functional derived in the previous section reduces to the ideal-gas form in the limit where the rod length vanishes. Before taking this limit it is convenient to introduce the *free density*

$$n(x,t,v) := \frac{f(x,t,v)}{1 - a\rho(x,t)}, \qquad \rho(x,t) = \int_{\mathbb{R}} dv\, f(x,t,v). \quad (3.22)$$

This quantity represents the velocity distribution per unit available length $(1 - a\rho)$, and is commonly used in the hydrodynamic description of hard rods. In these variables the effects of excluded volume are absorbed into the relation between f and n, while the resulting hydrodynamic evolution takes a simpler convective form, as we will see in the next section.

In the point-particle limit $a \to 0$ the excluded-volume correction vanishes and the free density reduces to the usual phase-space occupation function,

$$\lim_{a \to 0} n(x,t,v) = f(x,t,v). \quad (3.23)$$

We now examine the corresponding limit of the entropy functional. Using the expansion

$$\log(1 - a\rho) = -a\rho + O(a^2),$$

the configurational contribution becomes

$$-\Big(\frac{1}{a} - \rho\Big) \log(1 - a\rho) = \rho + O(a).$$

Hence, up to additive constants,

$$s(x,t) \xrightarrow[a \to 0]{} -k_B \int dv\, f(x,t,v) \log f(x,t,v) + k_B \rho(x,t) = -k_B \int dv\, f(x,t,v) \big(\log f(x,t,v) - 1\big), \quad (3.24)$$

which is the standard mixing entropy of an ideal classical gas (up to the usual coarse-graining conventions).

This result shows that the hard-rod entropy functional continuously connects to the ideal-gas entropy in the limit of vanishing rod length. In the following sections we will use this point-particle description to analyze the hydrodynamic evolution of the system.

3.4 Hydrodynamic Evolution and Boundary Conditions

At the Euler scale the dynamics of the coarse–grained phase-space distribution $f(x,t,v)$ is governed by a kinetic transport equation. This equation describes the ballistic propagation of quasiparticles together with the effects of collisions arising from the finite size of the rods.

3.4.1 Euler-scale transport equation

The hydrodynamic evolution of the velocity-resolved density $f(x,t,v)$ is given by [29]

$$\partial_t f(x,t,v) + \partial_x \big(v_{\text{eff}}[f](v)\, f(x,t,v)\big) = 0, \tag{3.25}$$

where $v_{\text{eff}}[f](v)$ denotes the effective propagation velocity of quasiparticles, which depends on the local distribution f. For notational simplicity, we will suppress the explicit functional dependence on f and write it as $v_{\text{eff}}(v)$, with the dependence on f implied.

3.4.2 Effective velocity

For a hard-rod gas the effective velocity depends on the local distribution through [29]

$$v_{\text{eff}}[f](v) = v + \frac{a}{1-a\rho} \int_{\mathbb{R}} dw\,(v-w) f(x,t,w), \tag{3.26}$$

where $\rho(x,t)$ is the local particle density and $u(x,t)$ is the local mean velocity, as defined in Section 3.1.

The effective velocity can be written in the equivalent form

$$v_{\text{eff}}(v) = \frac{v - a\rho u}{1-a\rho} \tag{3.27}$$

Physically, a tracer particle with bare velocity v experiences collisions with surrounding rods, which renormalize its propagation velocity to $v_{\text{eff}}(v)$.

3.4.3 Free density variables and point hard-rod limit

We introduce the free density given by equation 3.22, which represents the density per unit of available free length.

In terms of free density $n(x,t,v)$ the hydrodynamic equations take a simpler form. Using mass conservation one finds

$$\partial_t n(x,t,v) + v_{\text{eff}}(v)\,\partial_x n(x,t,v) = 0. \tag{3.28}$$

Thus the fields $n(x,t,v)$ behave as normal modes of the hard-rod fluid and propagate along characteristic trajectories with velocity $v_{\text{eff}}(v)$. The free density plays a role analogous to the quasiparticle occupation function in integrable quantum systems. In the point-particle limit $a \to 0$, the effective velocity reduces to the bare velocity, $v_{\text{eff}}(v) = v$.

3.4.4 Boundary conditions

In the point-particle limit $a \to 0$, quasiparticles propagate along straight-line trajectories, and boundary effects can be incorporated directly at the level of these trajectories.

We consider a finite system occupying the interval $[-N,0]$ connected to a reservoir at $x > 0$. A reflecting boundary is imposed at $x = -N$, while the interface at $x = 0$ acts as a localized defect.

The effect of boundaries is therefore implemented by specifying how trajectories are modified upon reaching $x = -N$ and $x = 0$.

At the left boundary $x = -N$, particles are perfectly reflected, corresponding to a reversal of velocity,

$$v \to -v. \tag{3.29}$$

Thus, trajectories undergo specular reflection at $x = -N$.

At the interface $x = 0$, quasiparticles are partially transmitted into the reservoir and partially reflected back into the system. This is encoded by assigning weights to trajectories: a quasiparticle crossing the defect is transmitted with probability $T(v)$ and reflected with probability $R(v)$, with

$$T(v) + R(v) = 1. \tag{3.30}$$

These coefficients determine the contribution of each trajectory in the construction of the solution. In particular, trajectories that undergo multiple reflections at the defect acquire factors of $R(v)$, while each transmission event contributes a factor of $T(v)$.

The full solution is obtained by summing over all trajectories consistent with these boundary processes, as described in the next subsection.

3.4.5 Point Hard-Rod Hydrodynamic Solutions

In the point-particle limit the transport equation can be solved analytically. We consider an initial state in which the system occupies the interval $[-N,0]$ while the reservoir is empty,

$$n_0(x,v) = g(v)\big[\theta(-x) - \theta(-x-N)\big], \tag{3.31}$$

where $g(v)$ is the momentum distribution. In our calculations we choose a Maxwell–Boltzmann distribution

$$g(v) = \frac{1}{\sqrt{2\pi\sigma^2}} \exp\left(-\frac{v^2}{2\sigma^2}\right). \tag{3.32}$$

with

$$\sigma^2 = \frac{k_B T}{m}$$

The full time-dependent solution is constructed by tracing quasiparticle trajectories and incorporating the boundary processes described in the previous subsection, including reflections at $x = -N$ and partial reflection and transmission at $x = 0$. Explicit expressions for the phase-space distribution $n_t(x,v)$ are obtained by summing over these image trajectories, as described in the cases below:

Case 1: Filled system, empty reservoir The system initially occupies the interval $[-N,0]$ while the reservoir is empty,

$$n_0(x,v) = g(v)[\theta(-x) - \theta(-x-N)]. \tag{3.33}$$

Each term in the sum corresponds to trajectories undergoing multiple reflections between the boundary and the defect, with factors R_v and T_v accounting for reflection and transmission events.

The time-evolved distribution on the system side ($x < 0$) is

$$\begin{aligned} n_t(x<0,v) = g(v)\Theta(v) \sum_{s=0}^{\infty} & R_v^s \left[\theta(-x-2sN+tv) - \theta(-x-2sN-2N+tv)\right] \\ + g(v)\Theta(-v) \sum_{s=0}^{\infty} \Big\{ & R_v^{s+1} \left[\theta(x-2sN-tv) - \theta(x-2sN-N-tv)\right] \\ + & R_v^s \left[\theta(-x+2sN+tv) - \theta(-x+2sN-N+tv)\right] \Big\}. \end{aligned} \tag{3.34}$$

On the reservoir side ($x > 0$) one obtains

$$n_t(x>0,v) = g(v)\Theta(v) \sum_{s=0}^{\infty} T_v R_v^s \left[\theta(-x-2sN+tv) - \theta(-x-2sN-2N+tv)\right]. \tag{3.35}$$

Case 2: Empty system, filled reservoir We now consider the opposite configuration where the reservoir $[0, L_{\text{res}}]$ is initially filled while the system is empty,

$$n_0(x,v) = g(v)\theta(x)\theta(L_{\text{res}} - x). \tag{3.36}$$

Particles can enter the system only if they move toward the defect, which corresponds to $v < 0$. The resulting distribution on the system side is

$$n_t(x<0,v) = g(v)\Theta(-v)\sum_{s=0}^{\infty} T_v R_v^s \Big[\theta(x_0)\theta(L_{\text{res}} - x_0) + \theta(x_1)\theta(L_{\text{res}} - x_1)\Big], \tag{3.37}$$

with

$$x_0 = -vt - (2sN - x), \qquad x_1 = -vt - (2(s+1)N + x). \tag{3.38}$$

The distribution on the reservoir side is

$$\begin{aligned} n_t(x>0,v) = {} & g(v)\theta(x - vt)\theta(L_{\text{res}} - (x - vt)) \\ & + g(v)R_v\theta(-x - vt)\theta(L_{\text{res}} - (-x - vt)) \\ & + g(v)\sum_{s=0}^{\infty} T_v^2 R_v^s \theta(-x - vt - 2sN)\theta(L_{\text{res}} - (-x - vt - 2sN)). \end{aligned} \tag{3.39}$$

Case 3: Closed system If the reservoir is absent the system is confined to the interval $[-N, 0]$ with reflecting boundaries. The hydrodynamic solution is

$$n_t(x,v) = g(v)\sum_{s=0}^{\infty} \left[\theta(-x - 2sN + tv) - \theta(-x - 2sN - N + tv)\right]. \tag{3.40}$$

General initial state The previous cases correspond to unit filling of either the system or the reservoir. For partially filled configurations the initial distribution can be written as

$$n_0(x,v) = \rho_S\, g(v)[\theta(-x) - \theta(-x - N)] + \rho_R\, g(v)\theta(x)\theta(L_{\text{res}} - x), \tag{3.41}$$

where ρ_S and ρ_R denote the initial filling fractions of the system and reservoir respectively, which satisfy

$$0 \le \rho_S, \rho_R \le 1.$$

Because the hydrodynamic equation is linear, the time–evolved distribution is simply the superposition

$$n_t(x,v) = \rho_S\, n_t^{(S)}(x,v) + \rho_R\, n_t^{(R)}(x,v), \tag{3.42}$$

where $n_t^{(S)}$ and $n_t^{(R)}$ denote the solutions of Case 1 and Case 2 respectively.

3.5 Hydrodynamic Entropy Dynamics

In this section we compute the hydrodynamic entropy using the phase-space distribution $f(x,t,v)$ obtained in the previous section. We first consider the point hard-rod limit ($a = 0$), where the solution is analytic, and then compare with finite hard rods.

The hydrodynamic entropy is computed from the phase-space distribution using the local entropy density derived earlier. In the point-particle limit, this reduces to

$$s(x,t) = -\int dv\, n(x,t,v) \log n(x,t,v) + \int dv\, n(x,t,v), \tag{3.43}$$

where $n(x,t,v)$ is the free density.

The system and reservoir entropies are obtained by integrating the entropy density over the corresponding spatial regions,

$$S^{(S)}_{\text{hydro}}(t) = \int_{-N}^{0} dx\, s(x,t), \qquad S^{(R)}_{\text{hydro}}(t) = \int_{0}^{L_{\max}} dx\, s(x,t). \tag{3.44}$$

These expressions are evaluated numerically using the analytic solutions for $n(x,t,v)$ obtained in the previous section. In the plots, we have taken $R = 1-\lambda^2, T = \lambda^2$, where $\lambda \in R$.

3.5.1 Point Hard-Rods: Filled System and Empty Reservoir

We first analyze the system entropy for Case 1 as shown in Fig. 3.1. As the variance σ increases, the peak value of the entropy also increases since a broader velocity distribution allows particles with higher momenta, resulting in a larger initial entropy. In all cases the entropy decreases with time as particles leave the subsystem and enter the reservoir. Larger values of σ lead to a faster decay since particles with higher velocities exit the subsystem more rapidly.

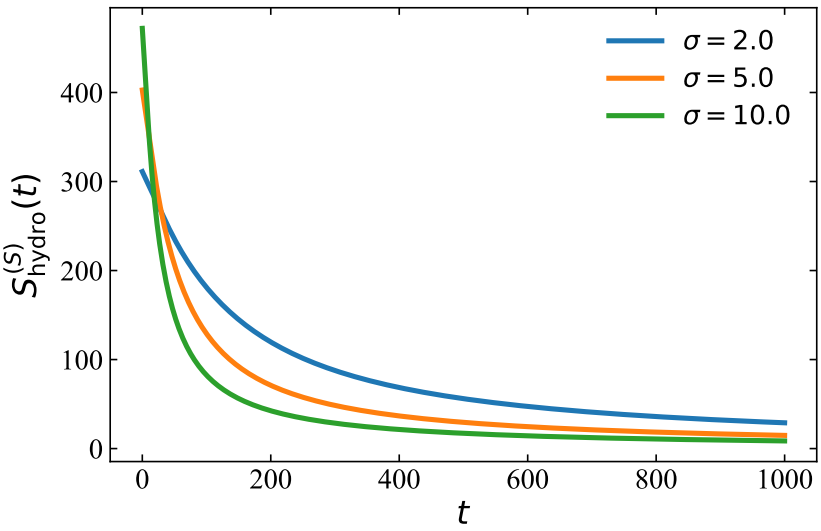

Figure 3.1: Hydrodynamic entropy of the system of point hard rods $S^{(S)}_{\text{hydro}}(t)$ vs time for some values of σ. Parameters used are $N = 100$ and $\lambda = 0.8$.

The time evolution of reservoir entropy for Case-1 is shown in Fig. 3.2

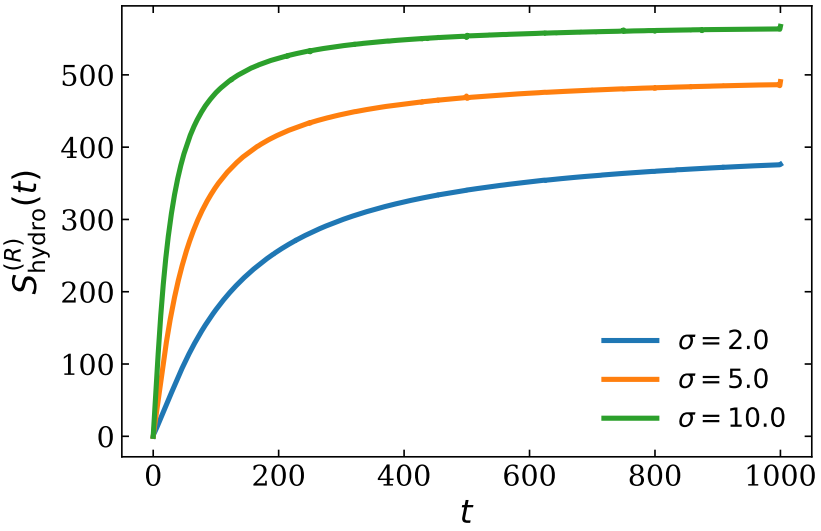

Figure 3.2: Hydrodynamic entropy of the reservoir of point hard rods $S^{(R)}_{\text{hydro}}(t)$ vs time for some values of σ. Parameters used are $N = 100$ and $\lambda = 0.8$, $L_{res} = 60000$

All plots begin with zero hydrodynamic entropy and increase with time until saturation. Higher σ results in a higher maximal entropy because of accessibility to higher momentum modes. This also results in faster entropy saturation.

Next, we examine the behavior of the total entropy of the system.

$$S^{(tot)}_{\text{hydro}}(t) = S^{(S)}_{\text{hydro}}(t) + S^{(R)}_{\text{hydro}}(t)$$

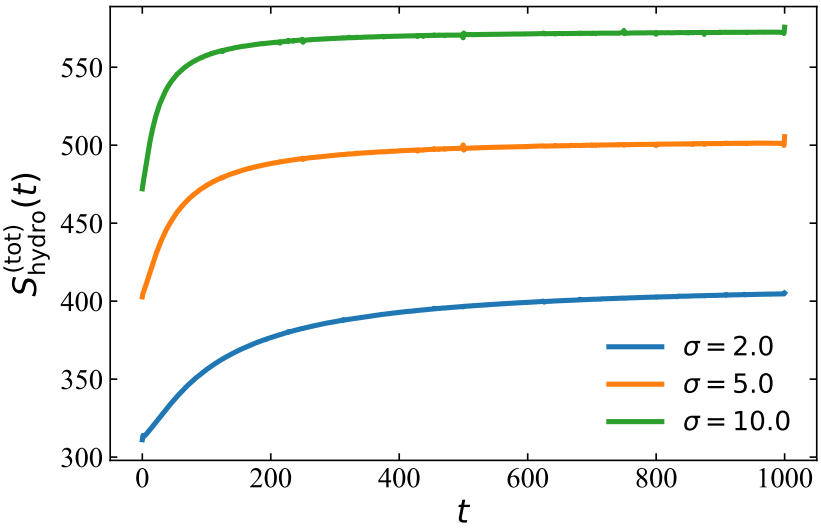

Figure 3.3: Total hydrodynamic entropy of the system of point hard rods $S^{(\text{tot})}_{\text{hydro}}(t)$ over time for different values of σ. The parameters used are $N = 100$, $\lambda = 0.8$, and $L_{\text{res}} = 60000$.

The total system entropy increases and approaches a steady finite value at long time. Larger σ has a larger initial growth. This indicates that the entropy generated during the transport process because of the defect saturates once the particle distribution becomes stationary. Now we move on to Case 2 of the point hard rods.

3.5.2 Point Hard-Rods: Empty System with Filled Reservoir

In this configuration the subsystem is initially empty and particles enter only through transmission across the defect. This leads to a non-monotonic entropy evolution: the subsystem entropy first increases as particles enter the system, reaches a maximum, and subsequently decreases as particles leave the subsystem again.

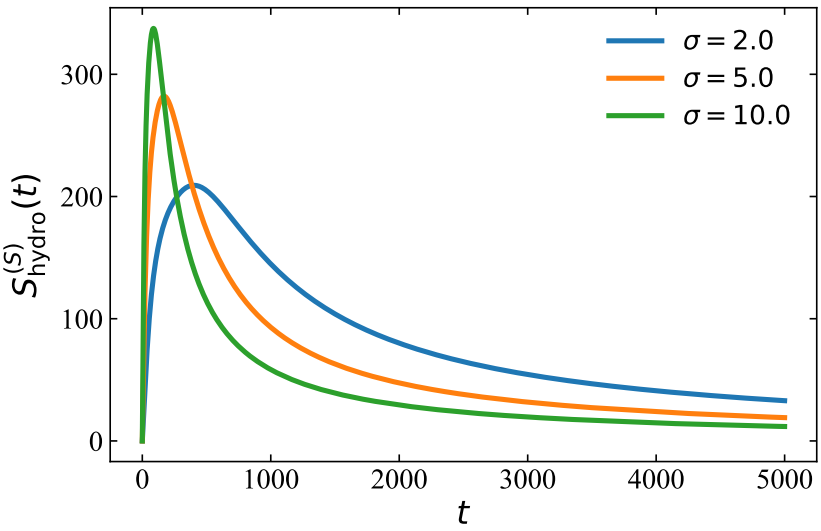

Figure 3.4: Hydrodynamic entropy of the system of point hard rods $S^{(S)}_{\text{hydro}}(t)$ vs time for different values of σ. Parameters used are $N = 100$, $\lambda = 0.8$, $L_{res} = 2000$

The initial entropy is zero as shown in the Fig. 3.4 because of absence of any particles. As more and more particles enter the system the entropy gradually increases, the early time growth is dependent on σ. After reaching a peak, the entropy gradually decreases because the particles start leaving the system again, and this results in the curve decaying to zero eventually.

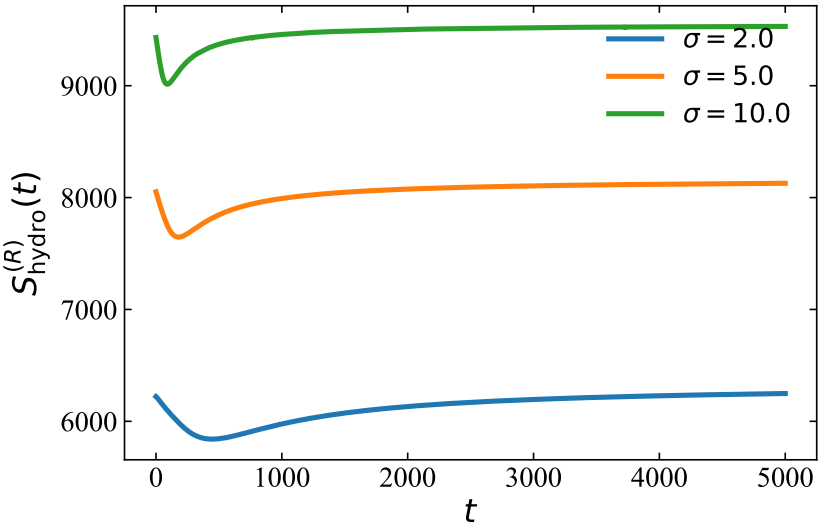

Figure 3.5: Hydrodynamic entropy of the reservoir of point hard rods $S^{(R)}_{\text{hydro}}(t)$ vs time for different values of σ. Parameters used are $N = 100$, $\lambda = 0.8$, $L_{\text{res}} = 2000$,

For this plot, the spatial integration domain is taken as $L_{\max} = L_{\text{res}} + v_{\max} t$, growing adaptively to contain all particle trajectories at each time step. Initially, the entropy starts from a high value and then decreases to reach the minimum as particles travel from the reservoir to the system. This corresponds to the same point which had a maximum for the system entropy.

After this particles begin to leave the subsystem again, leading to an increase in the reservoir entropy which eventually approaches a constant value at long times. Now we move to finite hard rods.

3.6 Finite Hard Rods

The hard rods have size $a > 0$. We highlight two specific cases: In the first case the reservoir size satisfies $L \gg N$, effectively acting as an infinite reservoir since particles do not reach the right boundary within the simulated time window. In the second case, we have a finite reservoir $L = 2N$ and there is also an additional right wall ensuring reflection back into the system, so all the hard rods remain in $[-N, L]$. For both cases, we have the distribution function $f_0 = \rho_0 g(v)[\theta(-x) - \theta(-x-N)]$, where ρ_0 is the initial particle density of the system as defined in earlier sections.

3.7 Numerical Implementation

The transport equation $\partial_t n + v_{\text{eff}}\,\partial_x n = 0$ is solved on a discrete grid of N_x spatial cells x_i ($i = 0, \ldots, N_x - 1$) and N_v velocity points v_k ($k = 0, \ldots, N_v - 1$), with time advancing in discrete steps labelled by superscript t. The effective velocity at spatial cell i and velocity mode k is

$$v_{\text{eff}}[i,k] = \frac{v_k - a\rho_i u_i}{1 - a\rho_i} \tag{3.45}$$

where $\rho_i = \int f(x_i, v, t)\,\mathrm{d}v$ is the local physical density, $u_i = \left(\int f(x_i, v, t)\, v\,\mathrm{d}v\right)/\rho_i$ is the local mean velocity, and f is related to n via

$$f = \frac{n}{1 + a n^{(0)}}, \qquad n^{(0)} = \int n\,\mathrm{d}v, \tag{3.46}$$

where $n^{(0)}$ is the zeroth velocity moment of n. This is the inverse of the free-density transformation $n = f/(1 - a\rho)$. The effective velocity $v_{\text{eff}}[i,k]$ is recomputed from the current density profile at every time step. Unlike the point-particle case, where the exact solution $n(x,v,t) = n_0(x - vt, v)$ is available, the hard-rod v_{eff} depends on the instantaneous local density $\rho(x,t)$ and mean velocity $u(x,t)$, making a closed-form solution unavailable.

The time evolution uses a first-order upwind scheme,

$$n^{t+\Delta t}[i,k] = n^t[i,k] - \frac{\Delta t}{\Delta x} \begin{cases} v_{\text{eff}}[i,k]\left(n[i,k] - n[i-1,k]\right) & v_{\text{eff}}[i,k] \geq 0, \\ v_{\text{eff}}[i,k]\left(n[i+1,k] - n[i,k]\right) & v_{\text{eff}}[i,k] < 0, \end{cases} \tag{3.47}$$

with an adaptive time step $\Delta t = \text{CFL} \times \Delta x / \max_{i,k} |v_{\text{eff}}[i,k]|$ and $\text{CFL} = 0.45$ is the Courant-Friedrichs-Lewy number, ensuring numerical stability.

At cells adjacent to a physical boundary, the upwind stencil requires a neighbouring value that lies outside the domain. This is supplied by a *ghost cell* — a fictitious cell placed just outside the boundary whose value is set by the boundary physics at each time step and used only in the flux computation.

Left wall ($x = -N$): Perfect reflection: $n_{\text{ghost}}[k] = n[0, k_{\text{ref}}[k]]$, where $k_{\text{ref}}[k] = N_v - 1 - k$ is the reflection index satisfying $v_{k_{\text{ref}}} = -v_k$, which follows from the symmetry of the uniform velocity grid about zero.

Defect ($x = 0$): The defect sits between cells i_L (last system cell) and i_R (first reservoir cell), with $f_{i_L}[k] \equiv f(x_{i_L}, v_k, t)$ and $f_{i_R}[k] \equiv f(x_{i_R}, v_k, t)$ denoting the physical distribution at the two cells immediately flanking the defect. Ghost distributions are constructed by applying the scattering rule to f,

$$f_{\text{ghost},i_L}[k] = R \cdot f_{i_L}[k_{\text{ref}}[k]] + T \cdot f_{i_R}[k], \qquad v_{\text{eff}}[i_L, k] < 0, \tag{3.48}$$

$$f_{\text{ghost},i_R}[k] = T \cdot f_{i_L}[k] + R \cdot f_{i_R}[k_{\text{ref}}[k]], \qquad v_{\text{eff}}[i_R, k] > 0, \tag{3.49}$$

where the first (second) term in each equation is the reflected (transmitted) contribution. These are converted back to n via $n = f/(1 - a\rho)$, where ρ is computed from the full interface distribution (both ghost and bulk modes) to correctly account for hard-rod exclusion at the boundary.

Right boundary: In Case 1 (infinite reservoir), no left-movers arrive from the reservoir at any time: the reservoir is initially empty and, in the absence of a right wall, no mechanism exists to reverse particle trajectories. Consequently $f_{i_R}[k] = 0$ for all modes with $v_k < 0$, and equations (3.48)–(3.49) reduce to

$$f_{\text{ghost},i_L}[k] = R \cdot f_{i_L}[k_{\text{ref}}[k]], \qquad v_{\text{eff}}[i_L, k] < 0, \tag{3.50}$$

$$f_{\text{ghost},i_R}[k] = T \cdot f_{i_L}[k], \qquad v_{\text{eff}}[i_R, k] > 0, \tag{3.51}$$

representing a single incoming stream from the system splitting into a reflected component re-entering the system and a transmitted component entering the reservoir. The right boundary at $x = L$ is absorbing ($n_{\text{ghost}} = 0$), with L chosen large enough that the density wavefront never reaches it within $t_{\max}$. In Case 2 (finite reservoir), the right wall at $x = 2N$ is perfectly reflecting, with ghost cell $n_{\text{ghost}}[k] = n[N_x - 1, k_{\text{ref}}[k]]$, identical in form to the left wall. This generates left-movers that return to the defect, activating the full two-sided scattering rule (3.48)–(3.49).

The entropy density

$$s(x_i, t) = -\int f \ln f \, \mathrm{d}v - \left(\tfrac{1}{a} - \rho_i\right) \ln(1 - a\rho_i) \tag{3.52}$$

is evaluated at each recorded time step, where f is recovered from n via equation (3.46). S_{sys} and S_{res} are obtained by spatial integration using the trapezoidal rule.

3.7.1 Finite Hard Rods: Infinite Reservoir

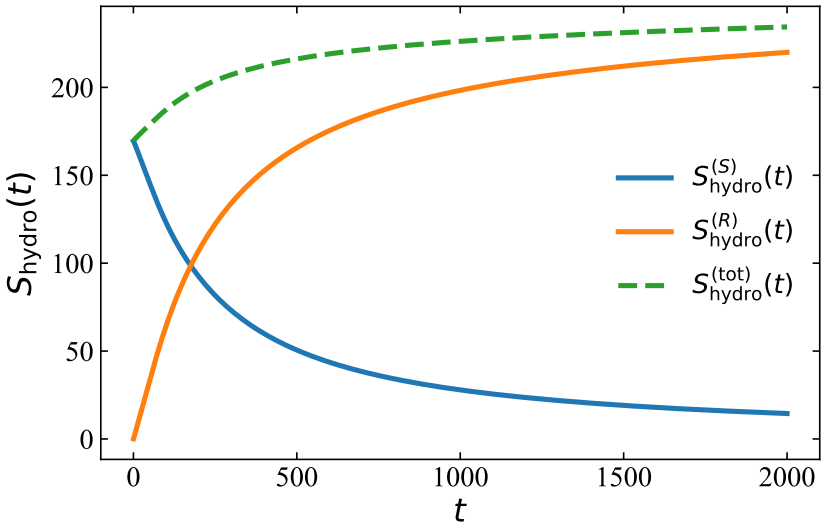

Figure 3.6: Hydrodynamic entropy of the system of finite hard rods over time for $\sigma = 1$. Parameters used are $N = 100$, $L = 20000$, $a = 0.2$, $\rho_0 = 0.6$, $T = 0.7$, $R = 0.3$

As shown in the Fig. 3.6, initially the reservoir entropy is zero, and the system entropy is maximal. As the system evolves, more and more hard rods leave the system so the entropy decreases with time and goes to zero. The reservoir entropy grows and saturates with time as does the total entropy.

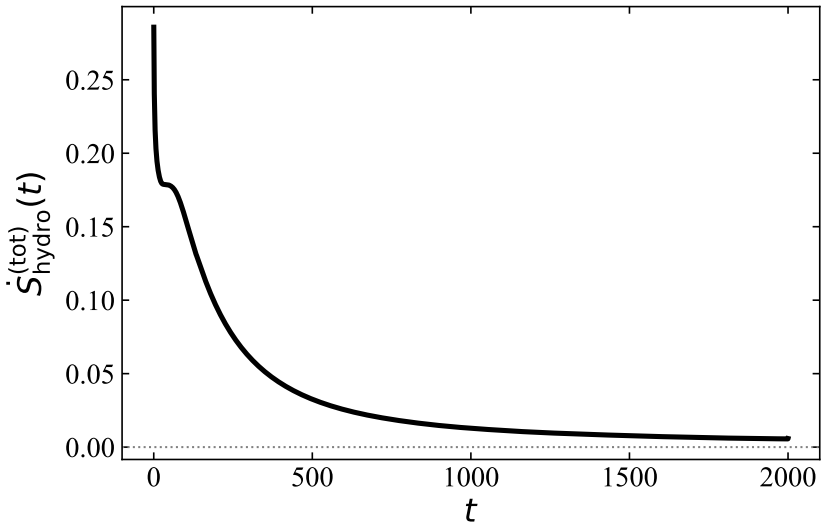

Figure 3.7: Rate of hydrodynamic entropy production of finite hard rods $\dot{S}^{(\text{tot})}_{\text{hydro}}(t)$ vs time for $\sigma = 1$. Parameters used are $N = 100$, $L = 20000$, $a = 0.2$, $\rho_0 = 0.6$, $T = 0.7$, $R = 0.3$

This plot shows the rate of hydrodynamic entropy production in the whole setup. $\dot{S}(t)$ remains non-negative, consistent with the Second Law of Thermodynamics and goes to zero at long time as all particles leak into the reservoir eventually.

Next we move to the finite reservoir case, where $L \sim 2N$.

3.7.2 Finite Hard Rods: Finite Reservoir

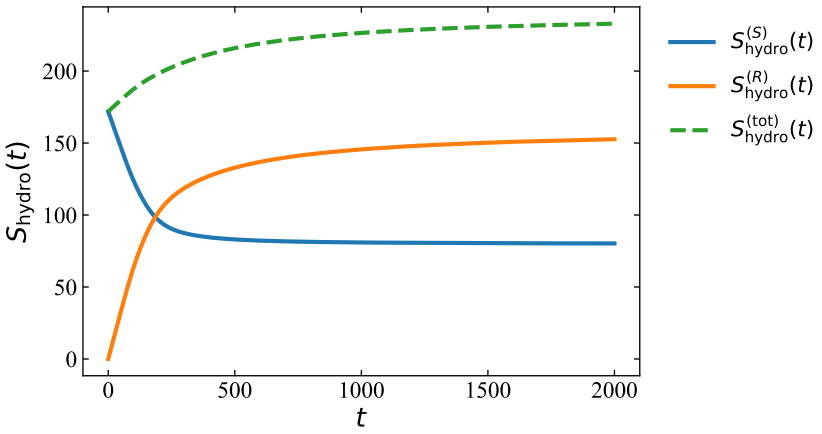

Figure 3.8: Hydrodynamic entropy of the system of finite hard rods $S^{(S)}_{\text{hydro}}(t)$ over time for $\sigma = 1$. Parameters used are $N = 100$, $L = 200$, $a = 0.2$, $\rho_0 = 0.6$, $T = 0.7$, $R = 0.3$

Unlike the one-sided case where entropy only ever flows out of the system, as the fig. 3.8 shows the system and reservoir will exchange particles back and forth through the defect, so both $S^{(S)}_{\text{hydro}}$ and $S^{(R)}_{\text{hydro}}$ should eventually equilibrate as the system reaches a steady state. The relative magnitude of $S^{(S)}_{\text{hydro}}$ and $S^{(R)}_{\text{hydro}}$ depends on the initial particle densities in the two regions. In the present setup, where the reservoir is initially empty, the system entropy initially dominates before equilibration.

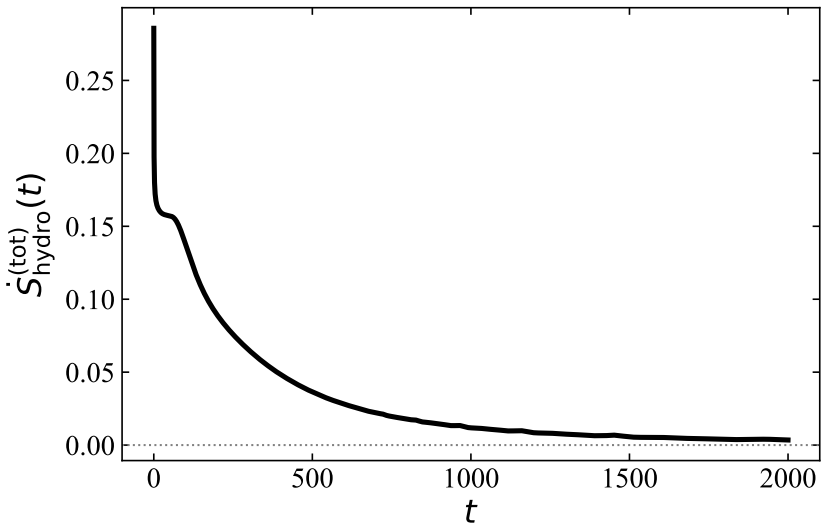

Figure 3.9: Rate of hydrodynamic entropy production of finite hard rods $\dot{S}^{(\mathrm{tot})}_{\mathrm{hydro}}(t)$ vs time for $\sigma = 1$. Parameters used are $N = 100$, $L = 200$, $a = 0.2$, $\rho_0 = 0.6$, $T = 0.7$, $R = 0.3$

The rate of hydrodynamic entropy production for the setup is more or less similar and remains non-negative.

The total hydrodynamic entropy in all the case approaches a finite value at late times. At the Euler scale, the bulk dynamics are advective and do not generate entropy [17, 29]. Therefore, entropy production is localized at the defect where particles are partitioned into transmitted and reflected components. Since the initial system contains a finite number of rods, the particle current through the defect vanishes asymptotically, causing the entropy production rate to decay to zero and the total entropy to saturate.

3.8 Summary

In this chapter we introduced the microscopic model of a classical hard-rod gas and derived the corresponding hydrodynamic entropy functional. The Euler-scale transport equation governing the coarse-grained phase-space distribution was then analyzed for a finite system coupled to a reservoir through a defect.

Analytical solutions were obtained in the point-particle limit, while finite hard rods were studied numerically by solving the hydrodynamic transport equation. The resulting entropy dynamics shows the transfer of entropy between the system and reservoir depending on the initial configuration, as well as entropy production associated with stochastic mixing at the defect.

These results provide the classical hydrodynamic counterpart to the quantum entropy dynamics studied in the previous chapter and set the stage for the comparison with classical information measures discussed in the next chapter.

Chapter 4

Mutual Information in Classical Systems

In this chapter we investigate the correlations between different regions of the classical hard rod system studied previously. To quantify these correlations we use classical mutual information, which measures the statistical dependence between two subsystems through their joint probability distribution.

We first introduce the general definition of mutual information and its formulation for phase–space fluctuations. We then compute the resulting correlation dynamics for different configurations, including Brownian diffusion with a semi-permeable interface, followed by non-interacting ballistic particles, and finite hard-rod systems. The analytical results are complemented by numerical simulations which allow us to compute the mutual information and analyze its time evolution.

4.1 Definition and General Framework

We begin by introducing the mutual information between two subsystems A and B, which quantifies the statistical dependence between their configurations.

Let X_A and X_B denote the microscopic configurations of particles in regions A and B, respectively. The statistical state of the system at time t is described by the joint probability density $P_t(X_A, X_B)$, with marginal distributions

$$P_{A,t}(X_A) = \int dX_B \, P_t(X_A, X_B), \tag{4.1}$$

$$P_{B,t}(X_B) = \int dX_A \, P_t(X_A, X_B). \tag{4.2}$$

The mutual information is defined as [31]

$$I(A:B;t) = \int dX_A \, dX_B \, P_t(X_A, X_B) \log \left[\frac{P_t(X_A, X_B)}{P_{A,t}(X_A) \, P_{B,t}(X_B)} \right]. \tag{4.3}$$

This quantity vanishes when the configurations in the two subsystems are statistically inde-

pendent.

An equivalent representation can be written in terms of Shannon differential entropies,

$$H[A] = -\int P_{A,t}(X_A)\,\log P_{A,t}(X_A)\,dX_A, \tag{4.4}$$

$$H[B] = -\int P_{B,t}(X_B)\,\log P_{B,t}(X_B)\,dX_B, \tag{4.5}$$

$$H[A,B] = -\int P_t(X_A,X_B)\,\log P_t(X_A,X_B)\,dX_A\,dX_B, \tag{4.6}$$

which leads to the identity

$$I(A:B;t) = H[A] + H[B] - H[A,B]. \tag{4.7}$$

4.2 Phase-Space Fluctuations and Occupation Statistics

We now discuss the statistical origin of the correlations between the system and the reservoir. The system is partitioned into two spatial regions and particles can move between them through the interface. Fluctuations in the particle distribution across this interface generate correlations between the two regions.

The microscopic configuration of the classical system consists of the phase-space coordinates (x_i, v_i) of all particles. The statistical state of the system at time t is described by the M-particle probability density (to avoid confusion with the system boundary at $x = -N$)

$$P_t(x_1,\ldots,x_M,v_1,\ldots,v_M).$$

In the present setup the spatial domain is divided into two regions, denoted A and B. Throughout this chapter we take $A = [-N,0]$, $B = (0,\infty)$, which correspond to the system and the reservoir respectively. The microscopic configuration can therefore be decomposed into the degrees of freedom belonging to each region, $X = (X_A,X_B)$ where X_A and X_B denote the particle coordinates located in regions A and B.

The mutual information introduced in Eq. (4.3) depends on the joint probability density $P_t(X_A,X_B)$ and its marginals

$$P_{A,t}(X_A) = \int dX_B\,P_t(X_A,X_B), \qquad P_{B,t}(X_B) = \int dX_A\,P_t(X_A,X_B).$$

Physically, $P_{A,t}(X_A)$ represents the probability density of observing a configuration X_A in region A, irrespective of the configuration in region B, and similarly for $P_{B,t}(X_B)$.

Since the configuration X_A specifies the particle coordinates in region A, it also determines the number of particles N_A occupying that region. Configurations with different values of N_A therefore correspond to distinct sectors of the configuration space. Hence, the marginal

distribution can be decomposed as

$$P_{A,t}(X_A) = \sum_{k=0}^{M} P(N_A = k)\, P(X_A \mid N_A = k) \tag{4.8}$$

This equation simply represents probability conservation over different particle number sectors and is equivalent to the marginal distribution defined above. Note that the time dependence is not always mentioned in $P(N_A = k)$ for a more compact notation.

The statistics of these sectors are determined by the single-particle occupation probabilities. For a particle initially located at y, the probability of being found in region A at time t is

$$p_A(y,t) = \int_A g(x,t|y)\, dx \tag{4.9}$$

while the probability of being in region B is

$$p_B(y,t) = \int_B g(x,t|y)\, dx \tag{4.10}$$

with $p_A(y,t) + p_B(y,t) = 1$. Here $g(x,t|y)$ denotes the single-particle propagator whose explicit form depends on the microscopic dynamics of the model under consideration.

In the following sections we study mutual information for several systems, beginning with the case of Brownian diffusion.

4.3 Brownian Diffusion with Semi-Permeable Membrane

4.3.1 Physical Setup

We consider a collection of M independent Brownian particles evolving in 1D in the presence of a reflecting wall at $x = -N$ and a semi-permeable membrane at $x = 0$. The spatial domain is partitioned into

$$A = (-N, 0), \qquad B = (0, \infty)$$

All particles initially start in region A at positions $y_i \in A$. The goal is to compute classical mutual information between the degrees of freedom in the two regions. Each particle undergoes overdamped diffusion with diffusion constant D. The interface at $x = 0$ allows partial transmission between the two regions and is characterized by a parameter κ.

4.3.2 Single-Particle Dynamics

We introduce the single particle propagator $g(x,t|y)$ defined on the domain $(-N, \infty)$ which satisfies the diffusion equation

$$\partial_t g(x,t|y) = D\,\partial_{xx} g(x,t|y) \tag{4.11}$$

with initial condition

$$g(x,0|y) = \delta(x-y), \qquad y \in A.$$

At the reflecting wall $x = -N$, we impose the Neumann boundary condition

$$\partial_x g(-N,t|y) = 0.$$

The single-particle propagator must satisfy

$$g_A(x,t|y) = g(x,t|y)\big|_{x<0} \quad , \quad g_B(x,t|y) = g(x,t|y)\big|_{x>0}$$

The interface conditions are

$$\partial_x g_A(0^-,t|y) = \partial_x g_B(0^+,t|y), \tag{4.12}$$

$$-D\,\partial_x g(0,t|y) = \kappa\left[g_A(0^-,t|y) - g_B(0^+,t|y)\right]. \tag{4.13}$$

The first condition expresses conservation of probability flux across the interface, so that the particles leaving system A reach system B. The second condition is a permeable boundary condition, which controls partial transmission with the parameter κ. The limits $\kappa = 0$ and $\kappa \to \infty$ correspond respectively to a perfectly reflecting interface and perfect transmission. In case of partially absorbing boundary conditions, the second term vanishes.

The explicit expression for the single-particle propagator can be derived using standard methods, as done in the Appendix E.

4.3.3 Occupation Probabilities

The occupation probabilities introduced in Section 4.2 can now be evaluated using the diffusion propagator.

$$p_A(y,t) = \int_{-N}^{0} g_A(x,t|y)\,dx,$$

and

$$p_B(y,t) = \int_{0}^{\infty} g_B(x,t|y)\,dx,$$

with $p_A(y,t) + p_B(y,t) = 1$ by probability conservation.

We also introduce conditional spatial densities

$$\rho_A(x,t|y) = \frac{g_A(x,t|y)}{p_A(y,t)}, \qquad x \in A \tag{4.14}$$

$$\rho_B(x,t|y) = \frac{g_B(x,t|y)}{p_B(y,t)}, \qquad x \in B \tag{4.15}$$

which are normalized within their respective regions.

4.3.4 Entropy Decomposition

Let X denote the particle position at time t with the probability density $g(x,t|y)$. Each particle can either be in region A or B as both are disjoint.

Therefore we introduce a discrete random variable R, which shows the region occupied by the particle.

$$R = R(X) = \begin{cases} A, & X \in A, \\ B, & X \in B. \end{cases}$$

We can also represent the position variable by

$$X = (R, X_R),$$

where X_R denotes the particle coordinate conditioned on the region. This representation is one-to-one: given X the pair (R,X_R) is uniquely determined, and conversely (R,X_R) uniquely reconstructs X. It is a simple reparameterization of the original random variable.

The Shannon entropy of the particle position is

$$H(X) = -\int g(x,t|y) \log g(x,t|y)\, dx \tag{4.16}$$

Applying the entropy chain rule to the decomposition $X = (R,X_R)$ yields

$$H(X) = H(R) + H(X_R|R), \tag{4.17}$$

where $H(R)$ is the entropy of the discrete region variable and $H(X_R|R)$ is the conditional entropy of the position within each region, which represents the spatial fluctuations in each region.

Using the decomposition of the probability density

$$g(x,t|y) = \begin{cases} p_A \rho_A(x,t|y), & x \in A, \\ p_B \rho_B(x,t|y), & x \in B, \end{cases}$$

where ρ_A and ρ_B are normalized conditional densities in the two regions, the entropy of the particle position becomes

$$H(X) = H(R) + p_A H(\rho_A) + p_B H(\rho_B) \tag{4.18}$$

A detailed derivation of this entropy decomposition is provided in Appendix F.

4.3.5 Mutual Information

We now consider the degrees of freedom localized in regions A and B as two subsystems. A single particle can occupy only one region at a time, so the spatial degrees of freedom in A and B do not fluctuate simultaneously.

The entropy associated with region A therefore contains two contributions: the uncertainty of whether the particle is in region A, and the conditional spatial entropy given that it is there. This gives

$$H_A^{\text{tot}} = H(R) + p_A H(\rho_A).$$

Similarly, the entropy associated with region B is

$$H_B^{\text{tot}} = H(R) + p_B H(\rho_B).$$

The full entropy of the particle position is

$$H_{AB} = H(R) + p_A H(\rho_A) + p_B H(\rho_B) \tag{4.19}$$

The mutual information between the two regions is defined as

$$I(A:B) = H_A^{\text{tot}} + H_B^{\text{tot}} - H_{AB} \tag{4.20}$$

Substituting the expressions above shows that the conditional spatial entropy terms cancel exactly, yielding

$$I(A:B) = H(R) = -p_A \log p_A - p_B \log p_B \tag{4.21}$$

Thus, for independent Brownian particles the mutual information between the two spatial regions is entirely determined by the occupation probability in each region. Spatial fluctuations within each region do not generate additional correlations between A and B.

For M independent particles starting at positions $\{y_i\}$, the mutual information is additive:

$$I(A:B)(t) = \sum_{i=1}^{M} \Big[- p_A(y_i,t) \log p_A(y_i,t) - p_B(y_i,t) \log p_B(y_i,t) \Big].$$

4.3.6 Numerical Scheme

The computation of mutual information requires evaluation of the occupation probabilities

$$p_A(y,t) = \int_{-N}^{0} g(x,t|y)\, dx, \tag{4.22}$$

from which the mutual information follows via the binary entropy formula. We consider two distinct numerical implementations corresponding to different physical setups.

Scheme I: Effective infinite-reservoir model

In this approach, the system is restricted to the domain $[-N,0]$ and the coupling to the reservoir is modeled through an absorbing (Robin) boundary condition at $x = 0$,

$$-D\,\partial_x g(0,t) = \kappa\, g(0,t). \tag{4.23}$$

The absorbing boundary condition is physically equivalent to coupling to an infinite reservoir: once a particle crosses $x = 0$ it propagates freely and never returns. We use $p_B = 1 - p_A$, which follows from probability conservation alone without requiring explicit integration over B.

The diffusion equation is solved numerically using a method-of-lines approach, in which space is discretized on a uniform grid while time evolution is handled using an implicit solver. The reflecting boundary at $x = -N$ is imposed via

$$\partial_x g(-N,t) = 0.$$

The initial condition is taken as a narrow Gaussian approximation to the delta function centered at y. The resulting propagator $g(x,t|y)$ is integrated numerically over the domain $[-N,0]$ to obtain $p_A(y,t)$.

The mutual information is then computed by summing the binary entropy contributions over all initial particle positions.

This scheme provides an efficient representation of diffusion into an effectively infinite reservoir, where particles do not return once they cross the boundary.

Scheme II: Finite reservoir with explicit membrane

In the second approach, the reservoir is treated explicitly by extending the domain to $[-N,L]$, with reflecting boundary conditions imposed at both ends,

$$\partial_x g(-N,t) = 0, \qquad \partial_x g(L,t) = 0.$$

The interface at $x = 0$ is modeled by a semi-permeable membrane satisfying

$$\partial_x g_A(0^-,t) = \partial_x g_B(0^+,t), \tag{4.24}$$

$$-D\,\partial_x g(0,t) = \kappa\,[g_A(0^-,t) - g_B(0^+,t)]. \tag{4.25}$$

The diffusion equation is solved using a Crank–Nicolson finite-difference scheme on a uniform spatial grid. The resulting discretization leads to a linear system of the form

$$A\,g^{n+1} = B\,g^n,$$

where the matrices A and B incorporate both diffusion and boundary conditions.

The interface conditions are implemented directly in this system, ensuring flux continuity and controlled transmission across the membrane.

In this formulation, total probability is conserved and particles can move between the system and reservoir in both directions.

Instead of evolving individual particles, the numerical scheme evolves a continuous density profile corresponding to an ensemble of independent particles initially distributed in region A. The occupation probabilities are obtained by integrating the density over the respective regions, and the mutual information is computed from the resulting probabilities.

Comparison of the two schemes

The two numerical approaches correspond to different physical limits. Scheme I provides an effective description of coupling to an infinite reservoir, where particles are irreversibly lost, leading to decay of mutual information at long times.

In contrast, Scheme II describes a finite closed system with conserved mass, where particles can move between the two regions and the mutual information approaches a non-zero equilibrium value determined by the relative sizes of the domains.

Together, these schemes allow us to probe both transient and steady-state aspects of information dynamics in diffusive systems.

4.3.7 Plots

We now illustrate the behavior of the mutual information for independent diffusing particles in the presence of a semi-permeable interface. The numerical results shown below correspond to different boundary conditions and reservoir configurations.

Case 1: Partially absorbing boundary conditions We consider a partially absorbing boundary in the interface of the system and the reservoir and plot the MI for this case.

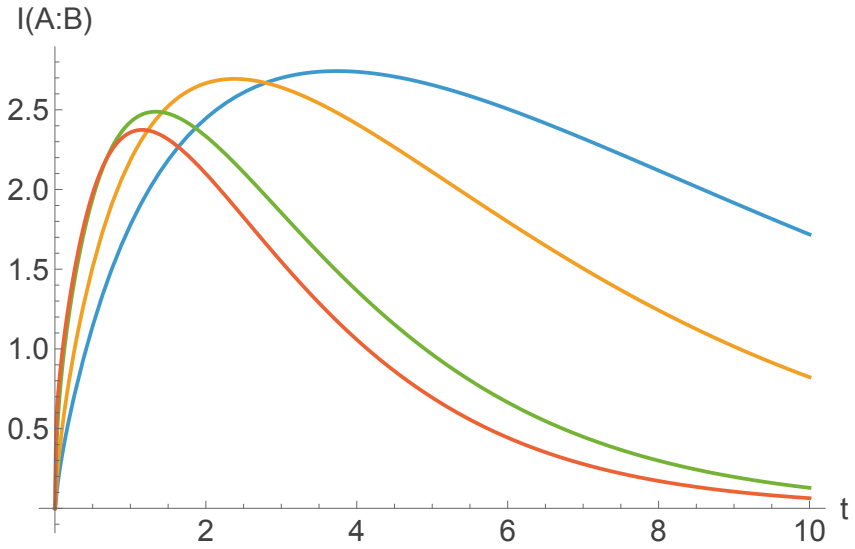

Figure 4.1: Mutual information $I(A:B)$ for $M=4$ Brownian particles; $\kappa = 0.5, 1, 5, 20$

The figure shows the mutual information $I(A:B)$ for $M=4$ Brownian particles for different values of the permeability κ. The parameter κ controls the strength of coupling between region A and region B. For smaller κ, particle escape is slower and the mutual information peak occurs at later times; it is also slightly higher because the information (or correlations) between the two regions is shared for a longer duration. As κ increases, particles escape more rapidly into region B, causing the mutual information to peak earlier and decay faster, indicating a quicker loss of correlations between the two regions. This setup effectively mimics coupling to an infinite reservoir, since particles crossing the boundary do not return to the system region.

Case 2: Partially transmitting boundary with a finite reservoir In this case, the system region A is coupled to a finite reservoir region B through a partially transmitting membrane at $x=0$ with permeability κ. The flux across the membrane is proportional to the density difference between the two sides, allowing particles to diffuse between the regions while conserving the total mass. Since both regions are finite with reflecting boundaries, particles eventually distribute uniformly across the entire domain. At equilibrium the probability of finding a particle in region A approaches the geometric ratio

$$p_A \to \frac{N}{N+L},$$

where N and L denote the lengths of regions A and B respectively. Consequently, the mutual information approaches the constant value given by the binary entropy

$$I(A:B) = -p_A \log p_A - (1-p_A)\log(1-p_A).$$

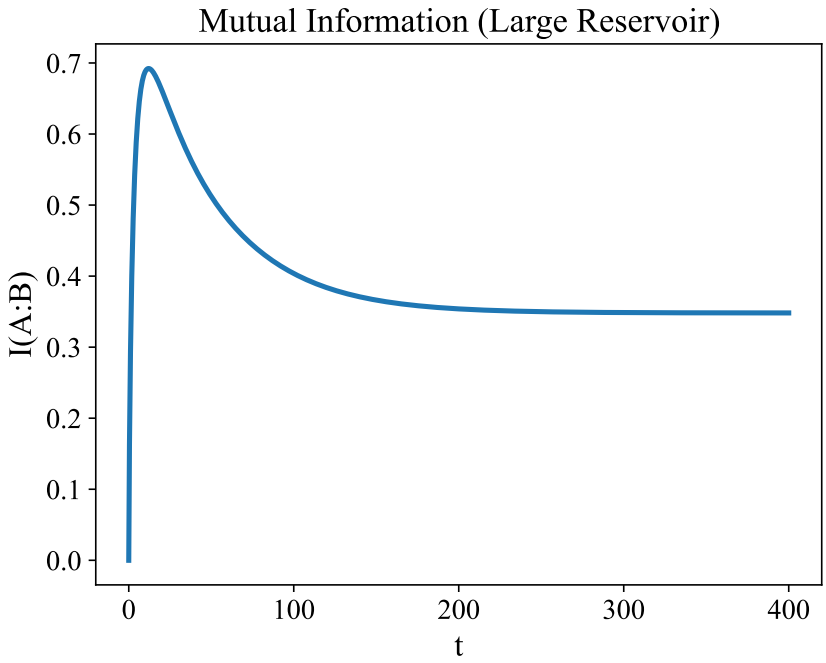

Figure 4.2: Mutual information $I(A:B)$ for diffusion across a partially transmitting membrane with a finite reservoir; $N = 8$, $L = 40$.

Figure 4.2 shows the time evolution of the mutual information for the finite reservoir setup. Starting from an initially localized configuration in region A, the mutual information grows as particles diffuse through the membrane and the uncertainty in the particle number in region A increases. The mutual information reaches a maximum at intermediate times when the fluctuations in N_A are largest. At longer times the system relaxes toward equilibrium and the mutual information approaches the constant value predicted by the geometric ratio $p_A = N/(N+L)$. We now move to ballistic non-interacting particles.

4.4 Ballistic Non-Interacting Particles

We consider M non-interacting particles undergoing ballistic motion, with deterministic trajectories $x_i(t) = x_i(0) + v_i(0)t$ and velocities drawn independently from a Maxwell–Boltzmann distribution. The corresponding single-particle propagator is

$$g_{\mathrm{bal}}(x,t|y) = \frac{1}{\sqrt{2\pi\sigma_v^2 t^2}} \exp\left(-\frac{(x-y)^2}{2\sigma_v^2 t^2}\right). \tag{4.26}$$

Since the particles evolve independently and no ordering constraints are present, the general derivation of Section 4.3 applies directly with g_{bal} replacing the diffusion propagator. The

mutual information is therefore given by

$$I(A:B,t)=\sum_{i=1}^{M}\Big[-p_A(y_i,t)\log p_A(y_i,t)-p_B(y_i,t)\log p_B(y_i,t)\Big],$$

where $p_A(y_i,t)=\int_A g_{\rm bal}(x,t|y_i)\,dx$ and $p_B(y_i,t)=1-p_A(y_i,t)$.

Thus, ballistic dynamics does not introduce any new features beyond those already captured in the Brownian analysis. We remark that the exact form of $g_{\rm bal}(x,t|y)$ would be modified in the presence of a defect at $x=0$, but the structure of the mutual information remains unchanged.

We now turn to the classical hard rod system introduced in the previous chapter. In contrast to the Brownian case, correlations between the two regions arise from the excluded-volume interaction and the resulting ordering constraints between particles.

4.5 Finite Hard Rods

We consider M hard rods of length a evolving in one dimension, in the presence of a reflecting wall at $x=-N$ and a partially transmitting defect at $x=0$. We derive the mutual information between the spatial regions

$$A=[-N,0],\qquad B=(0,\infty)$$

from the exact microscopic joint probability distribution. We note that the analysis for point hard rods is also the same, only with the limit $a\to 0$.

4.5.1 Coordinate Mapping and Ordered Configuration Space

Let $x_1,\dots,x_M$ denote the rod centers satisfying the hard-core constraint

$$x_1<x_2-a<\cdots<x_M-(M-1)a.$$

It is convenient to introduce the coordinate map [23, 24]

$$q_i=x_i-(i-1)a,$$

which transforms the system into ordered point particles

$$q_1<q_2<\cdots<q_M.$$

The Jacobian of this transformation is unity, and the configuration space becomes the ordered simplex

$$S_M=\{q_1<\cdots<q_M\}.$$

This mapping removes the hard-core constraint by compressing the excluded volume, at the cost of introducing a nontrivial permutation structure in the probability distribution.

The spatial partition translates into q-coordinates as

$$x_i < 0 \iff q_i < -(i-1)a.$$

This index-dependent boundary arises from the excluded volume shift and must be retained in all subsequent calculations. It is equivalent to the uniform physical boundary $x_i < 0$ in real space.

4.5.2 Exact Joint Probability Distribution

Let

$$\tilde{g}_i(q,t) = \int du\, g(q,u,t \mid q_{i0}, u_{i0})$$

denote the single-particle position propagator obtained from the transport equation with reflecting wall and stochastic defect.

Because hard rods interact only through excluded volume, the hard-rod mapping reduces the dynamics to ordered point particles in the compressed coordinates q_i. Collisions between rods correspond to exchanges of particle labels, which leads to a sum over permutations of independent propagators.

The exact M-particle joint probability density in q-space is therefore

$$P_q(\mathbf{q},t) = \left(\sum_{\sigma \in S_M} \prod_{i=1}^{M} \tilde{g}_i(q_{\sigma(i)}, t) \right) \mathbf{1}_{q_1 < \cdots < q_M}.$$

Here S_M denotes the permutation group of M elements, and the indicator function $\mathbf{1}_{q_1<\cdots<q_M}$ restricts the density to the ordered sector. Outside this sector the probability density vanishes.

The sum over permutations encodes the exchange of particle labels due to collisions and is the fundamental source of correlations in the system.

4.5.3 Number Distribution Across the Partition

Let $A = [-N, 0]$ denote the region to the left of the defect. We define the number of rods in A as

$$N_A = \sum_{i=1}^{M} \mathbf{1}_{x_i<0}.$$

Using the coordinate mapping,

$$x_i < 0 \iff q_i < -(i-1)a.$$

Because the coordinates are ordered ($q_1 < \cdots < q_M$), the particles in region A always form a contiguous block $\{q_1, \ldots, q_k\}$ for some k.

The probability that exactly k rods lie in A is therefore

$$P(N_A = k) = \int_{\Omega_k} P_q(\mathbf{q}, t)\, d^M q,$$

where the integration domain is

$$\Omega_k = \{q_1 < \cdots < q_M\} \cap \{q_k < -(k-1)a\} \cap \{q_{k+1} > -ka\},$$

This domain implements the physical condition that exactly the first k ordered particles lie to the left of the boundary $x = 0$.

The above integral over the ordered simplex determines the full number distribution.

4.5.4 Conditional Structure and Residual Correlations

As discussed in the previous subsection, fixing the occupation number $N_A = k$ restricts the ordered coordinates to the sector

$$\Omega_k = \{q_1 < \cdots < q_M\} \cap \{q_k < -(k-1)a\} \cap \{q_{k+1} > -ka\},$$

where the binding constraints $q_k < -(k-1)a$ and $q_{k+1} > -ka$ ensure that exactly the first k coordinates satisfy $x_i = q_i + (i-1)a < 0$, with all remaining ordering constraints propagating automatically from $q_1 < \cdots < q_M$.

Within this sector the coordinates naturally separate into those belonging to region A, namely $q_1, \ldots, q_k$, and those belonging to region B, namely $q_{k+1}, \ldots, q_M$.

However, this separation of coordinates does *not* imply factorization of the probability density. The joint distribution is given by

$$P_q(\mathbf{q}, t) = \left(\sum_{\sigma \in S_M} \prod_{i=1}^{M} \tilde{g}_i(q_{\sigma(i)}, t) \right) \mathbf{1}_{q_1 < \cdots < q_M}$$

Specifically, permutations σ that assign label $i \leq k$ to a position q_j with $j > k$ generate cross-terms of the form $\tilde{g}_i(q_j)\, \tilde{g}_j(q_i)$ coupling A-coordinates to B-coordinates. As a result, even within a fixed sector Ω_k, the configurations in the two regions remain statistically correlated.

Therefore, in general,

$$P(X_A, X_B \mid N_A = k) \neq P(X_A \mid N_A = k)\, P(X_B \mid N_B = M - k).$$

The full joint probability distribution can be decomposed as

$$P(X_A, X_B) = \sum_{k=0}^{M} P(N_A = k)\, P(X_A, X_B \mid N_A = k),$$

which follows from the law of total probability.

The marginal distributions are similarly given by

$$P_A(X_A) = \sum_{k=0}^{M} P(N_A = k)\, P(X_A \mid N_A = k),$$

$$P_B(X_B) = \sum_{k=0}^{M} P(N_B = M-k)\, P(X_B \mid N_B = M-k).$$

Since $N_A = N_A(X_A)$ is a deterministic function of the microscopic configuration X_A, one simply counts the rod centres satisfying $x_i < 0$. The conditional density satisfies $P(X_A \mid N_A = k) = 0$ whenever $N_A(X_A) \neq k$, so only the single term $k = N_A(X_A)$ contributes.

4.5.5 Mutual Information Decomposition

We now derive the structure of the mutual information explicitly. Using the decomposition expression from earlier subsection, we obtain

$$\begin{aligned} \frac{P(X_A, X_B)}{P_A(X_A)\, P_B(X_B)} &= \frac{P(N_A = k)\, P(X_A, X_B \mid N_A = k)}{P(N_A = k)\, P(X_A \mid N_A = k) \cdot P(N_B = M-k)\, P(X_B \mid N_B = M-k)} \\ &= \frac{1}{P(N_A = k)} \cdot \frac{P(X_A, X_B \mid N_A = k)}{P(X_A \mid N_A = k)\, P(X_B \mid N_B = M-k)}. \end{aligned} \tag{4.27}$$

Taking the logarithm,

$$\log \frac{P(X_A, X_B)}{P_A(X_A)\, P_B(X_B)} = -\log P(N_A = k) + \log \frac{P(X_A, X_B \mid N_A = k)}{P(X_A \mid N_A = k)\, P(X_B \mid N_B = M-k)}. \tag{4.28}$$

Substituting (4.28) into the definition (4.3), and noting that $k = N_A(X_A)$ varies across the integration domain, we decompose the domain into disjoint sectors $\{\Omega_k\}_{k=0}^{M}$ on each of which k is constant,

$$I(A:B) = \sum_{k=0}^{M} \int_{\Omega_k} dX_A\, dX_B\, P(X_A, X_B) \left[-\log P(N_A = k) + \log \frac{P(X_A, X_B \mid N_A = k)}{P(X_A \mid N_A = k)\, P(X_B \mid N_B = M-k)} \right]. \tag{4.29}$$

Within each sector Ω_k, substituting $P(X_A, X_B) = P(N_A = k)\, P(X_A, X_B \mid N_A = k)$ and using the

normalization $\int_{\Omega_k} P(X_A, X_B \mid N_A = k)\, dX_A\, dX_B = 1$, the first term gives

$$-\sum_{k=0}^{M} P(N_A = k) \log P(N_A = k) = H(N_A)$$

This is the Shannon entropy of the particle-number distribution.

The second term is identified as the conditional mutual information between the configurations in the two regions given $N_A = k$,

$$I(X_A : X_B \mid N_A = k) = \int_{\Omega_k} dX_A\, dX_B\, P(X_A, X_B \mid N_A = k) \log \frac{P(X_A, X_B \mid N_A = k)}{P(X_A \mid N_A = k)\, P(X_B \mid N_B = M - k)}$$

Thus, the mutual information decomposes as

$$I(A : B) = H(N_A) + \sum_{k=0}^{M} P(N_A = k)\, I(X_A : X_B \mid N_A = k).$$

This decomposition separates two distinct contributions:

- the entropy $H(N_A)$ arising from fluctuations in the number of particles across the interface,
- a conditional mutual information term $I(X_A : X_B \mid N_A = k)$, arising from mixed permutations in the joint PDF which captures residual correlations within each sector.

Computing the second term requires integrating the full M-body conditional distribution over the $2M$-dimensional sector Ω_k, a task not reducible to single-particle propagators and analytically intractable in closed form. We therefore compute $H(N_A)$, which captures correlations arising from particle-number fluctuations across the defect and is fully determined by the single-particle propagators $\tilde{g}_i$.

4.5.6 Calculation of the Number Distribution

As shown in the previous subsection, the mutual information can be decomposed into a contribution from particle-number fluctuations and an additional contribution arising from correlations within each sector.

We focus on the particle-number contribution, which is determined by the distribution $P(N_A = k)$. This quantity can be computed directly from the microscopic joint probability distribution.

Using the ordered-coordinate representation,

$$P_q(\mathbf{q}, t) = \left(\sum_{\sigma \in S_M} \prod_{i=1}^{M} \tilde{g}_i(q_{\sigma(i)}, t) \right) \mathbf{1}_{q_1 < \cdots < q_M},$$

the probability that exactly k rods lie in region A is obtained by integrating over the sector

$$\Omega_k = \{q_1 < \cdots < q_M\} \cap \{q_k < -(k-1)a\} \cap \{q_{k+1} > -ka\},$$

giving

$$P(N_A = k) = \int_{\Omega_k} P_q(\mathbf{q}, t)\, d^M q.$$

The functions $\tilde{g}_i(q,t)$ are the single-particle position propagators obtained from the phase-space propagator $g(x,u,t|x_0,u_0)$ by integrating over velocities. The many-body distribution is constructed from these propagators along with the permutation sum, which encodes the effects of collisions.

The derivation of the propagator $\tilde{g}_i$ for the reflecting wall at $x = -N$ and the partially transmitting defect at $x = 0$ is presented in Appendix G.

4.5.7 Numerical Scheme

The particle-number distribution $P(N_A = k, t)$ is computed by explicitly enumerating the discrete configurations generated by the single-particle propagator derived in Appendix G. The procedure follows directly from the structure of the propagator.

For each particle i with initial condition (q_{i0}, u_{i0}), the position propagator $\tilde{g}_i(q,t)$ at time t is represented as a finite set of weighted peaks $\{(q_{i,\alpha}, w_{i,\alpha})\}$, corresponding to all admissible trajectories with defect encounter times $t_s \leq t$. For particles with initial velocity $u_{i0} < 0$, the particle first reflects elastically off the wall at $q = -N$ before reaching the defect; the peak enumeration accounts for this initial wall reflection before applying the defect scattering rules.

The many-body configurations are constructed by selecting one peak for each particle and considering all permutations of particle labels. For each choice of peaks and each permutation $\sigma \in S_M$, the configuration

$$\mathbf{q} = (q_{\sigma(1)}, \ldots, q_{\sigma(M)})$$

is retained only if it satisfies the global ordering constraint $q_1 < \cdots < q_M$, implementing the indicator function $\mathbf{1}_{q_1 < \cdots < q_M}$ in the joint PDF. The corresponding joint weight is

$$w(\mathbf{q}) = \prod_{i=1}^{M} w_{i,\alpha_i},$$

where w_{i,α_i} denotes the weight of the peak selected from particle i, implementing the product of single-particle propagators in the microscopic joint distribution.

For each valid ordered configuration $\mathbf{q}$, the occupation number in region A is computed as

$$N_A(\mathbf{q}) = \sum_{j=1}^{M} \mathbf{1}_{q_j < -(j-1)a},$$

using the hard-rod coordinate mapping $x_j = q_j + (j-1)a$. The number distribution is then obtained by accumulating weights over all configurations with fixed occupation number,

$$P(N_A = k, t) = \sum_{\mathbf{q}: N_A(\mathbf{q}) = k} w(\mathbf{q}).$$

Finally, the number-fluctuation contribution to the mutual information is computed as

$$H(N_A, t) = -\sum_{k=0}^{M} P(N_A = k, t) \log P(N_A = k, t).$$

The computation involves a sum over all combinations of single-particle peaks and permutations, with cost scaling factorially in M, restricting exact evaluation to small system sizes.

4.5.8 Numerical Results for Finite Systems

Using the numerical scheme described above, the number distribution $P(N_A = k, t)$ is evaluated exactly, allowing the leading contribution to the mutual information to be computed as

$$H(N_A, t) = -\sum_{k=0}^{M} P(N_A = k, t) \log P(N_A = k, t).$$

We now present the time evolution of this quantity for finite systems with particle numbers $M = 2, \ldots, 6$.

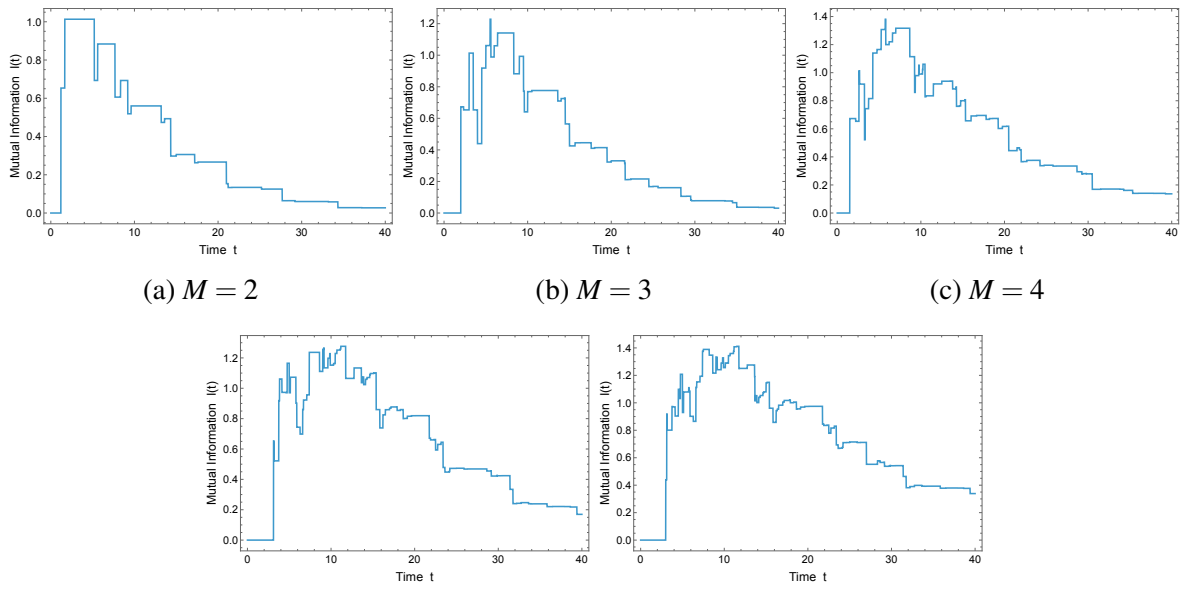

(a) $M = 2$ (b) $M = 3$ (c) $M = 4$

(d) $M = 5$ (e) $M = 6$

Figure 4.3: Time evolution of $H(N_A,t)$, the dominant contribution to the mutual information $I(A:B,t)$, for finite hard-rod systems. The number of configurations grows factorially with M, limiting the exact evaluation to $M \leq 6$.

These figures show the time evolution of the particle-number contribution to the mutual information, given by the Shannon entropy $H(N_A)$, for a finite system with M rods ($M = 2,\ldots,6$). At $t = 0$ the configuration of particles is completely known, and therefore the occupation number N_A is fixed. The number distribution is thus sharply peaked and $H(N_A) = 0$. In this limit, the full mutual information vanishes as well.

Over time, particles move from the system to the reservoir. This introduces uncertainty in the number of particles located in region A, broadening the distribution $P(N_A = k,t)$. Consequently, $H(N_A)$ increases from zero and reaches a maximum at intermediate times. As the particle number increases, the peak value becomes larger, reflecting the greater number of possible particle-number configurations in the subsystem. A broader distribution of N_A leads to a larger entropy and therefore a larger value of $H(N_A)$. The time at which the maximum occurs also shifts slightly to later times, since a larger number of particles must be transmitted through the defect before the uncertainty in N_A becomes maximal.

At later times the particles transmit through the defect and move away from region A. The occupation number distribution again becomes sharply peaked and $H(N_A)$ correspondingly decreases towards zero. In the present setup with an infinite reservoir, the occupation number becomes deterministic at long times, so that $H(N_A) \to 0$. Naturally, the mutual information also vanishes, $I(A:B) \to 0$.

4.6 Summary

In this chapter we studied the mutual information between two spatial regions of classical particle systems separated by an interface. We first introduced the general definition of mutual information in terms of the joint probability distribution of microscopic configurations.

For Brownian diffusion with a semi-permeable interface, the particles are independent but each occupies only one region at a time; the mutual information is therefore exactly equal to the Shannon entropy of the discrete region variable, $I(A:B) = H(R)$, determined entirely by the occupation probabilities. For non-interacting ballistic particles the mutual information has the same structure, with the ballistic propagator g_{bal} replacing the diffusion propagator.

For the hard-rod system, the ordering constraint and the permutation structure of the joint PDF prevent an exact closed-form result. Starting from the exact microscopic joint distribution, we derived the decomposition

$$I(A:B) = H(N_A) + \sum_{k=0}^{M} P(N_A = k)\, I(X_A : X_B \mid N_A = k),$$

where $H(N_A)$ captures correlations arising from particle-number fluctuations across the defect and the second term encodes residual microscopic correlations within each occupation sector. Since $I(X_A : X_B \mid N_A = k) \geq 0$ for every k, $H(N_A)$ is an exact lower bound on the full mutual information. The correction term is not analytically tractable, as it requires the full M-body conditional distribution and is not reducible to single-particle propagators. We therefore computed $H(N_A)$ exactly using the discrete peak structure of the ballistic propagator. Numerical results for $M = 2,\ldots,6$ illustrate the growth, peak, and decay of $H(N_A,t)$ over time, with the peak value and timescale both increasing with the number of particles.

Chapter 5

Discussion

The results presented in this work investigate the relationships among transport, entropy, and correlations in integrable many-body systems coupled to a reservoir via a partially transmitting defect. Two microscopic models were considered: a quantum system of free fermions and a classical gas of hard rods. For both systems, the dynamics were studied at two complementary levels of description: the microscopic evolution of the underlying particles and the Euler-scale hydrodynamic description provided by generalized hydrodynamics. Although the hydrodynamic equations governing transport take similar forms in these models, the physical interpretation of entropy and correlations differs significantly between the quantum and classical cases. In particular, this work reproduces the microscopic and hydrodynamic entropy dynamics of a fermionic system coupled to a reservoir and extends the analysis to classical hard-rod gases in order to compare thermodynamic entropy with information-theoretic measures of correlations.

Generalized hydrodynamics describes integrable fluids in terms of quasi-particle densities that propagate ballistically through the system. At the Euler scale, these equations govern the transport of conserved quantities. In this regime, the entropy density satisfies a local continuity equation, implying that entropy is transported with the quasiparticle flow rather than being generated in the bulk at the Euler scale.

For the fermionic system, the microscopic dynamics were analyzed using the correlation-matrix formalism, which allows for the exact computation of the von Neumann entanglement entropy. In parallel, the hydrodynamic entropy was obtained using the generalized hydrodynamics framework. A comparison of the two descriptions shows excellent agreement between the microscopic entanglement entropy and the hydrodynamic prediction. This agreement is consistent with the quasiparticle picture of entanglement spreading in integrable quantum systems, in which pairs of entangled quasiparticles propagate ballistically through the system and carry both thermodynamic entropy and quantum correlations. The late-time decay of the entropy follows a power-law behavior whose exponent depends on the form of the reflection coefficient $R(k)$. Since the defect is introduced phenomenologically in the present setup, different choices of $R(k)$ primarily modify the late-time scaling behavior while leaving the qualitative hydrodynamic picture and the structure of the entropy dynamics unchanged.

The classical hard-rod gas exhibits a qualitatively different microscopic interpretation. In this system, the hydrodynamic density represents a coarse-grained phase-space description of particle configurations, and the entropy reflects the configurational disorder of this particle distribution. When particles encounter the partially transmitting defect, they are reflected or transmitted with fixed probabilities. This stochastic scattering introduces mixing between particles originating from the system and the reservoir, leading to uncertainty in the number of particles remaining in the subsystem and constituting the source of entropy production, while the bulk dynamics remain purely advective at the Euler scale.

The correlations generated by this stochastic process can be quantified through the mutual information between the system and the reservoir. In the hard-rod system, the structure of the joint probability distribution prevents an exact factorization, and the mutual information does not admit a closed-form expression. Instead, it can be decomposed into a contribution arising from particle-number fluctuations and a conditional contribution encoding residual correlations within each occupation sector. The particle-number term provides a lower bound on the full mutual information, while the conditional term remains analytically intractable and depends on the full many-body distribution.

The dynamics of the particle-number contribution display a rise-and-fall structure that resembles the qualitative shape of a Page curve. Initially, the particle number in the subsystem is fixed and the mutual information therefore vanishes. As particles are transmitted through the defect, fluctuations in the particle number increase and this contribution grows. At late times, the behavior depends on the system configuration: in the presence of an effectively infinite reservoir the mutual information decays to zero, while in finite systems it saturates to a non-zero value. Although this behavior resembles the qualitative features of the Page curve observed in quantum systems, its origin is purely classical, arising from stochastic particle-number fluctuations rather than quantum entanglement.

A related observation arises in the case of Brownian particles, where the stochastic dynamics lead to a particularly simple structure for the correlations between the system and the reservoir. In this case, the mutual information reduces to a binary entropy associated with the probability of a particle being located in either region. In a finite system with reflecting boundaries the long-time distribution of particles approaches a uniform equilibrium state. As a result, the probability of finding a particle in the subsystem approaches the geometric ratio determined by the sizes of the two regions, and the mutual information saturates at a constant value given by the corresponding binary entropy. In contrast, when the subsystem is coupled to an effectively infinite reservoir, for example through partially absorbing (Robin) boundary conditions, particles that leave the system do not return and the occupation probability of the subsystem eventually vanishes. In this case the mutual information exhibits a rise-and-fall behavior analogous to a Page curve. This provides a simple example in which correlations generated by stochastic transport can be expressed directly in terms of the Shannon entropy of a two-outcome process.

These results highlight an important distinction between thermodynamic entropy and information-theoretic measures of correlations. Hydrodynamic descriptions retain only coarse-grained information about local densities and currents. Consequently, while hydrodynamics successfully captures the transport of thermodynamic entropy, it does not encode the microscopic correlations responsible for the mutual information dynamics observed in the classical system. Furthermore, the hydrodynamic equations do not distinguish between the transport of quasiparticles in the quantum system and the transport of classical coarse-grained particle distributions. Although the mathematical structure of the transport equations may be similar, the physical interpretation of entropy and correlations can therefore differ substantially.

5.1 Limitations

Some limitations of the present analysis should be noted.

The numerical calculations necessarily involve finite system sizes and finite observation times, which limit direct access to the asymptotic regime. In particular, the exact evaluation of the mutual information in the classical hard-rod system requires the computation of the full probability distribution of particle configurations. The number of possible configurations grows factorially with particle number, making direct enumeration computationally expensive. In the present work, the calculations were therefore restricted to particle numbers up to $N = 6$, beyond which the computational cost increases significantly.

The hydrodynamic description employed in this work is restricted to the Euler scale and therefore neglects subleading corrections such as diffusive effects. While this approximation captures the leading ballistic transport of conserved quantities, it does not account for fluctuations and broadening effects that may become relevant at longer times or in more refined descriptions.

In the classical hard-rod system, the analysis of correlations was restricted to the contribution arising from particle-number fluctuations, which provides a lower bound on the full mutual information. The remaining conditional contribution, which encodes correlations within each occupation sector, was not evaluated due to its dependence on the full many-body distribution. This term cannot be expressed in terms of single-particle propagators and requires access to the full joint distribution.

Chapter 6

Conclusion

This thesis investigated the relationship between transport, entropy, and correlations in integrable many-body systems coupled to a reservoir through a partially transmitting defect. Using both microscopic calculations and Euler-scale hydrodynamic descriptions, we analyzed entropy and correlation dynamics in a quantum system of free fermions and a classical gas of hard rods.

The results show that hydrodynamic entropy accurately reproduces the large-scale behavior of entanglement entropy in the fermionic system, while in the classical hard-rod model correlations arise from stochastic particle-number fluctuations generated by the defect. Although the resulting particle-number contribution to the mutual information displays a Page-curve-like structure, its origin is purely classical and differs fundamentally from quantum entanglement.

These findings highlight an important distinction between thermodynamic entropy and information-theoretic measures of correlations: while hydrodynamic descriptions capture entropy transport, they do not encode the microscopic correlation structures present in many-body systems.

Future work could focus on extending the classical analysis to larger particle numbers using more efficient numerical or sampling methods, as well as developing approaches to estimate the conditional contributions to the mutual information. It would also be of interest to explore more general settings, including different defect dynamics or non-integrable systems, in order to further clarify the relationship between classical correlations and quantum entanglement.

Appendix A

Derivation of Reflection and Transmission Coefficients

In this appendix we derive the reflection and transmission coefficients for the local defects introduced in Chapter 2 by solving the single-particle scattering problem for the tight-binding Hamiltonian.

The scattering state is written as

$$\psi_n = \begin{cases} e^{ikn} + r_k e^{-ikn}, & n \leq 0, \\ t_k e^{ikn}, & n \geq 1, \end{cases} \qquad E = -2g\cos k, \tag{A.1}$$

where r_k and t_k denote the reflection and transmission amplitudes.

The amplitudes are obtained by imposing the time-independent Schrödinger equation at the defect sites.

A.1 Conformal Defect

For the conformal defect the modified couplings at the junction are

$$h_{0,1} = h_{1,0} = -g_c, \qquad h_{0,0} = -h_{1,1} = \sqrt{g^2 - g_c^2}. \tag{A.2}$$

Applying the Schrödinger equation at sites $n = 0$ and $n = 1$ gives

$$E\,\psi_0 = -g\,\psi_{-1} - g_c\,\psi_1 + \sqrt{g^2 - g_c^2}\,\psi_0, \tag{A.3}$$

$$E\,\psi_1 = -g_c\,\psi_0 - g\,\psi_2 - \sqrt{g^2 - g_c^2}\,\psi_1. \tag{A.4}$$

Using the scattering ansatz

$$\psi_{-1} = e^{-ik} + r_k e^{ik}, \quad \psi_0 = 1 + r_k, \quad \psi_1 = t_k e^{ik}, \quad \psi_2 = t_k e^{i2k}, \tag{A.5}$$

and solving the resulting equations yields

$$t_k = \lambda, \qquad r_k = \pm\sqrt{1-\lambda^2}, \qquad \lambda = \frac{g_c}{g}. \tag{A.6}$$

Therefore

$$T_k = |t_k|^2 = \lambda^2, \qquad R_k = |r_k|^2 = 1-\lambda^2. \tag{A.7}$$

A.2 Hopping Defect

For the hopping defect only the hopping across the junction is modified,

$$h_{0,1} = h_{1,0} = -g_c. \tag{A.8}$$

The Schrödinger equation at the defect sites becomes

$$E\psi_0 = -g\,\psi_{-1} - g_c\,\psi_1, \tag{A.9}$$

$$E\psi_1 = -g_c\,\psi_0 - g\,\psi_2. \tag{A.10}$$

Substituting the scattering ansatz gives

$$E(1+r_k) = -g(e^{-ik} + r_k e^{ik}) - g_c t_k e^{ik}, \tag{A.11}$$

$$Et_k e^{ik} = -g_c(1+r_k) - g t_k e^{i2k}. \tag{A.12}$$

Solving for r_k and t_k using $E = -2g\cos k$ yields

$$t_k = \frac{2igg_c \sin k}{g_c^2 - g^2 e^{2ik}}, \qquad r_k = \frac{g_c^2 - g^2}{g_c^2 - g^2 e^{2ik}}. \tag{A.13}$$

The reflection and transmission probabilities are therefore

$$R_k = \frac{(\lambda^2-1)^2}{\lambda^4 + 1 - 2\lambda^2\cos(2k)}, \qquad T_k = 1 - R_k, \tag{A.14}$$

where $\lambda = g_c/g$.

A.3 Density Defect

For the density defect the hopping amplitudes remain unchanged while the on-site potentials are modified,

$$h_{0,0} = h_{1,1} = g_c. \tag{A.15}$$

The Schrödinger equation at the defect sites becomes

$$E\psi_0 = -g\,\psi_{-1} - g\,\psi_1 + g_c\,\psi_0, \tag{A.16}$$

$$E\psi_1 = -g\,\psi_0 - g\,\psi_2 + g_c\,\psi_1. \tag{A.17}$$

Substituting the scattering ansatz gives

$$E(1+r_k) = -g(e^{-ik} + r_k e^{ik}) - g t_k e^{ik} + g_c(1+r_k), \tag{A.18}$$

$$E t_k e^{ik} = -g(1+r_k) - g t_k e^{i2k} + g_c t_k e^{ik}. \tag{A.19}$$

Solving for the amplitudes yields the reflection probability

$$R_k = \frac{\lambda^2(\lambda - 2\cos k)^2}{2 + 2\lambda^2 + \lambda^4 - 4\lambda^3\cos k + 2(\lambda^2 - 1)\cos(2k)}, \tag{A.20}$$

with

$$T_k = 1 - R_k, \qquad \lambda = \frac{g_c}{g}. \tag{A.21}$$

Appendix B

Derivation of the Entanglement Entropy Formula

In this appendix we derive the relation between the entanglement entropy of a subsystem and the eigenvalues of its correlation matrix for Gaussian fermionic states. It is based on the work by [26]

B.1 Gaussian Structure of the Reduced Density Matrix

For a quadratic fermionic Hamiltonian the many-body state is Gaussian, meaning that all higher-order correlation functions can be expressed in terms of two-point correlators via Wick's theorem.

If the global state is Gaussian, the reduced density matrix of a subsystem A obtained by tracing out its complement $\bar{A}$

$$\rho_A = \mathrm{Tr}_{\bar{A}}\rho \tag{B.1}$$

is also Gaussian. It can therefore be written as the exponential of a quadratic operator,

$$\rho_A = \frac{1}{Z_A}\exp\left(-\sum_{i,j\in A} h_{ij}\, c_i^\dagger c_j\right), \tag{B.2}$$

where h_{ij} defines the entanglement Hamiltonian.

B.2 Diagonalization of the Correlation Matrix

The reduced density matrix is completely determined by the subsystem correlation matrix

$$C_{ij} = \langle c_i^\dagger c_j\rangle, \qquad i,j \in A. \tag{B.3}$$

Since C is Hermitian it can be diagonalized as

$$C = U^\dagger \Lambda U, \tag{B.4}$$

where

$$\Lambda = \mathrm{diag}(m_1, m_2, \ldots, m_N) \tag{B.5}$$

The unitary matrix U defines new fermionic operators

$$a_\ell = \sum_{i \in A} U_{\ell i} c_i, \tag{B.6}$$

which diagonalize the correlation matrix,

$$\langle a_\ell^\dagger a_{\ell'} \rangle = m_\ell \delta_{\ell\ell'}. \tag{B.7}$$

B.3 Factorization of the Reduced Density Matrix

In the basis of the entanglement modes a_ℓ, the reduced density matrix becomes diagonal and factorizes into independent fermionic degrees of freedom,

$$\rho_A = \prod_{\ell=1}^{N_A} \rho_\ell, \tag{B.8}$$

where

$$\rho_\ell = \frac{e^{-\varepsilon_\ell a_\ell^\dagger a_\ell}}{1 + e^{-\varepsilon_\ell}}. \tag{B.9}$$

Each entanglement mode therefore behaves as an independent fermionic two-level system.

B.4 Occupation Number Representation

In the occupation-number basis $\{|0\rangle, |1\rangle\}$ of the fermionic mode ℓ, the reduced density matrix takes the form

$$\rho_\ell = \frac{1}{1 + e^{-\varepsilon_\ell}} \begin{pmatrix} 1 & 0 \\ 0 & e^{-\varepsilon_\ell} \end{pmatrix}. \tag{B.10}$$

The average occupation of the mode is therefore

$$m_\ell = \langle a_\ell^\dagger a_\ell \rangle = \mathrm{Tr}(a_\ell^\dagger a_\ell \rho_\ell) = \frac{e^{-\varepsilon_\ell}}{1 + e^{-\varepsilon_\ell}} = \frac{1}{e^{\varepsilon_\ell} + 1}. \tag{B.11}$$

This relation can be inverted to obtain

$$\varepsilon_\ell = \ln\left(\frac{1 - m_\ell}{m_\ell}\right). \tag{B.12}$$

B.5 Entanglement Entropy

The von Neumann entropy of the subsystem is

$$S_A = -\mathrm{Tr}(\rho_A \ln \rho_A). \tag{B.13}$$

Since $\rho_A = \bigotimes_\ell \rho_\ell$, the entropy is additive over the modes,

$$S_A = \sum_{\ell=1}^{N_A} S_\ell, \tag{B.14}$$

where

$$S_\ell = -\mathrm{Tr}(\rho_\ell \ln \rho_\ell). \tag{B.15}$$

Evaluating the trace for the two-level density matrix gives

$$S_\ell = -m_\ell \ln m_\ell - (1-m_\ell)\ln(1-m_\ell). \tag{B.16}$$

Summing over all modes yields

$$S_A = -\sum_{\ell=1}^{N_A} \left[m_\ell \ln m_\ell + (1-m_\ell)\ln(1-m_\ell) \right], \tag{B.17}$$

which is the result used in the main text.

Appendix C

Derivation of the Current Operator

In this appendix we derive the expression for the particle current across the junction between the subsystem and the reservoir.

C.1 Heisenberg Equation of Motion

The particle number operator at site i is

$$\hat{n}_i = \hat{c}_i^\dagger \hat{c}_i. \tag{C.1}$$

Its time evolution follows from the Heisenberg equation

$$\frac{d\hat{n}_i}{dt} = i[\hat{H}, \hat{n}_i]. \tag{C.2}$$

For the quadratic Hamiltonian

$$\hat{H} = \sum_{j,k} h_{jk} \hat{c}_j^\dagger \hat{c}_k, \tag{C.3}$$

one finds

$$[\hat{H}, \hat{n}_i] = \sum_j \left(h_{ij} \hat{c}_i^\dagger \hat{c}_j - h_{ji} \hat{c}_j^\dagger \hat{c}_i \right). \tag{C.4}$$

Therefore

$$\frac{d\hat{n}_i}{dt} = i \sum_j \left(h_{ij} \hat{c}_i^\dagger \hat{c}_j - h_{ji} \hat{c}_j^\dagger \hat{c}_i \right). \tag{C.5}$$

C.2 Current Across the Junction

At the junction between sites 0 and 1, the hopping amplitude is $h_{01} = h_{10} = -g_c$. The time evolution of $\hat{n}_0$ therefore involves only this term, leading to the identification of the current operator

$$\hat{I}_{0\to 1} = i g_c \left(\hat{c}_0^\dagger \hat{c}_1 - \hat{c}_1^\dagger \hat{c}_0 \right). \tag{C.6}$$

Taking expectation values gives the average current

$$I(t) = \langle \hat{I}_{0\to 1} \rangle = 2g_c \,\mathrm{Im}\left[\langle \hat{c}_0^\dagger(t)\hat{c}_1(t)\rangle\right]. \tag{C.7}$$

Using the definition of the correlation matrix,

$$C_{ij}(t) = \langle \hat{c}_i^\dagger(t)\hat{c}_j(t)\rangle, \tag{C.8}$$

the current can be written as

$$I(t) = 2g_c \,\mathrm{Im}[C_{01}(t)]. \tag{C.9}$$

Appendix D

Entropy Increase under Defect-Induced Mixing

In this appendix we show that the hard-rod entropy functional increases under the mixing induced by a defect that reflects and transmits particles with probabilities R, T satisfying $R+T=1$.

D.1 Entropy functional

The local thermodynamic entropy density of the hard-rod gas is

$$s(f,\rho) = -\int_{\mathbb{R}} dv\, f(v)\log f(v) - \left(\frac{1}{a}-\rho\right)\log(1-a\rho), \tag{D.1}$$

where

$$\rho = \int_{\mathbb{R}} dv\, f(v). \tag{D.2}$$

It is convenient to write

$$s(f,\rho) = s_{\text{vel}}(f) + s_{\text{conf}}(\rho), \tag{D.3}$$

with

$$s_{\text{vel}}(f) = -\int dv\, f\log f, \qquad s_{\text{conf}}(\rho) = -\left(\frac{1}{a}-\rho\right)\log(1-a\rho). \tag{D.4}$$

D.2 Mixing at the defect

Let $f_L(v)$ and $f_R(v)$ denote the velocity distributions arriving at the defect from the left and right. After scattering the outgoing distribution is

$$f_m(v) = Rf_L(v) + Tf_R(v), \qquad R,T \geq 0, \qquad R+T=1. \tag{D.5}$$

The corresponding density is

$$\rho_m = R\rho_L + T\rho_R, \tag{D.6}$$

where $\rho_{L,R} = \int dv\, f_{L,R}(v)$.

D.3 Velocity entropy

Define

$$\phi(x) = -x\log x. \tag{D.7}$$

Since

$$\phi''(x) = -\frac{1}{x} < 0, \tag{D.8}$$

the function ϕ is strictly concave. The velocity entropy can therefore be written

$$s_{\text{vel}}(f) = \int dv\, \phi(f(v)). \tag{D.9}$$

Using Jensen's inequality for concave functions,

$$\phi(Rx+Ty) \geq R\phi(x) + T\phi(y), \tag{D.10}$$

we obtain

$$s_{\text{vel}}(f_m) \geq Rs_{\text{vel}}(f_L) + Ts_{\text{vel}}(f_R), \tag{D.11}$$

with equality only if $f_L(v) = f_R(v)$.

D.4 Configurational entropy

Define

$$g(\rho) = -\left(\frac{1}{a} - \rho\right)\log(1-a\rho), \qquad 0 \leq \rho < \frac{1}{a}. \tag{D.12}$$

A direct computation gives

$$g''(\rho) = -\frac{a}{1-a\rho} < 0, \tag{D.13}$$

so $g(\rho)$ is strictly concave. Applying Jensen's inequality yields

$$s_{\text{conf}}(\rho_m) \geq Rs_{\text{conf}}(\rho_L) + Ts_{\text{conf}}(\rho_R), \tag{D.14}$$

with equality only when $\rho_L = \rho_R$.

D.5 Total entropy

Combining the two inequalities gives

$$s(f_m, \rho_m) \geq Rs(f_L, \rho_L) + Ts(f_R, \rho_R). \tag{D.15}$$

Equality holds only if

$$f_L(v) = f_R(v) \quad \text{and} \quad \rho_L = \rho_R. \tag{D.16}$$

D.6 Interpretation

The defect mixes the incoming velocity distributions according to

$$f_m = Rf_L + Tf_R. \tag{D.17}$$

Since the hard-rod entropy functional is concave in both f and ρ, such mixing necessarily increases the entropy unless the two distributions are identical. Repeated scattering events therefore generate entropy until the velocity distributions on both sides coincide, at which point entropy production ceases.

Appendix E

Calculation of Green's function for a Brownian particle with a square barrier

In this appendix, we derive the single-particle propagator for a brownian particle with a square barrier. There are many analytical methods of solving the Fokker-Planck equation with the specific boundary conditions [32] but we follow the Laplace Transform approach.

We compute the propagator $g(x,t|y)$ for an overdamped Brownian particle diffusing on the semi-infinite domain $x \in [-N,\infty)$ with a reflecting wall at $x = -N$ and a localized defect at $x = 0$ modeled by a narrow square barrier potential supported on $[0,\varepsilon]$.

E.1 Brownian dynamics and Fokker–Planck equation

We consider overdamped Langevin dynamics in an external potential $U(x)$,

$$dX_t \;=\; -\mu U'(X_t)\,dt + \sqrt{2D}\,dW_t, \tag{E.1}$$

where D is the diffusion constant, μ is the mobility, and W_t is a Wiener process. The associated Fokker–Planck (Smoluchowski) equation for the propagator $g(x,t|y)$ reads

$$\partial_t g(x,t|y) \;=\; -\partial_x J(x,t|y), \qquad J(x,t|y) \;=\; -D\,\partial_x g(x,t|y) - \mu U'(x)\,g(x,t|y). \tag{E.2}$$

Equivalently,

$$\partial_t g(x,t|y) \;=\; \partial_x\big(D\,\partial_x g(x,t|y) + \mu U'(x)\,g(x,t|y)\big)\,. \tag{E.3}$$

The initial condition is

$$g(x,0|y) = \delta(x-y). \tag{E.4}$$

E.2 Wall and defect condition

The reflecting wall at $x = -N$ imposes zero probability flux:

$$J(-N,t|y) = 0. \tag{E.5}$$

The defect at $x = 0$ is implemented energetically via a square barrier potential on $[0,\varepsilon]$.

Remark: A defect could alternatively be modeled by a δ-localised drift term in the Fokker–Planck equation. However, we observed that such a perturbation doesn't lead to partial reflection and transmission as we needed. Therefore, in order to obtain a physically transparent partially transmitting interface consistent with detailed balance, we instead model the defect as a narrow square potential barrier of height U_0 and width ε.

E.3 Square barrier potential profile

We choose the following piecewise constant potential profile:

$$U(x) = \begin{cases} 0, & -N \le x < 0, \\ U_0, & 0 < x < \varepsilon, \\ 0, & x > \varepsilon, \end{cases} \qquad U_0 > 0. \tag{E.6}$$

We denote $\beta = (k_B T)^{-1}$ and the Boltzmann factor

$$\alpha := e^{-\beta U_0} \in (0,1]. \tag{E.7}$$

Since $U'(x) = 0$ in each open interval $(-N,0)$, $(0,\varepsilon)$, and (ε,∞), the propagator satisfies the pure diffusion equation in each region.

E.4 Piecewise formulation

We decompose the propagator into three pieces

$$g(x,t|y) = \begin{cases} g_1(x,t|y), & -N \le x < 0, \\ g_2(x,t|y), & 0 < x < \varepsilon, \\ g_3(x,t|y), & x > \varepsilon. \end{cases} \tag{E.8}$$

In each region,

$$\partial_t g_i(x,t|y) = D\,\partial_{xx} g_i(x,t|y), \qquad i = 1,2,3. \tag{E.9}$$

We focus on the physically relevant case where the initial point lies in the "system" part,

$$y \in (-N, 0), \tag{E.10}$$

so that the initial conditions are

$$g_1(x,0|y) = \delta(x-y), \qquad g_2(x,0|y) = 0, \qquad g_3(x,0|y) = 0. \tag{E.11}$$

Reflecting wall. Since $U'(x) = 0$ in region 1, the flux is simply $J = -D\partial_x g_1$, thus

$$\partial_x g_1(-N,t|y) = 0. \tag{E.12}$$

Matching at $x = 0$ and $x = \varepsilon$. Because $U(x)$ is discontinuous at $x = 0$ and $x = \varepsilon$, one must impose:

1. continuity of the flux J (probability conservation),

2. the Boltzmann-weighted continuity across a potential step.

In the present piecewise constant case the flux continuity reduces to continuity of $\partial_x g$ at each interface, since $U'(x) = 0$ in the bulk of each region.

At $x = 0$ we impose

$$g_2(0^+,t|y) = \alpha\, g_1(0^-,t|y), \qquad \partial_x g_2(0^+,t|y) = \partial_x g_1(0^-,t|y). \tag{E.13}$$

At $x = \varepsilon$ we impose

$$g_3(\varepsilon^+,t|y) = \alpha^{-1}\, g_2(\varepsilon^-,t|y), \qquad \partial_x g_3(\varepsilon^+,t|y) = \partial_x g_2(\varepsilon^-,t|y). \tag{E.14}$$

Finally, normalizability of the probability density implies the decay condition

$$g_3(x,t|y) \to 0 \qquad (x \to +\infty). \tag{E.15}$$

E.5 Laplace transform in time

We introduce the Laplace transform

$$\widehat{g}_i(x,s|y) := \int_0^\infty e^{-st}\, g_i(x,t|y)\, dt, \qquad s > 0, \qquad i = 1,2,3. \tag{E.16}$$

With the bulk diffusion equation (E.9) and initial conditions (E.11), the Laplace-transformed equations become

$$D\,\partial_{xx}\widehat{g}_1(x,s|y) - s\,\widehat{g}_1(x,s|y) = -\delta(x-y), \qquad -N < x < 0, \tag{E.17}$$

$$D\,\partial_{xx}\widehat{g}_2(x,s|y) - s\,\widehat{g}_2(x,s|y) = 0, \qquad 0 < x < \varepsilon, \tag{E.18}$$

$$D\,\partial_{xx}\widehat{g}_3(x,s|y) - s\,\widehat{g}_3(x,s|y) = 0, \qquad x > \varepsilon. \tag{E.19}$$

We define

$$\kappa := \sqrt{\frac{s}{D}} > 0. \tag{E.20}$$

E.6 General solutions in each region

Region 3 ($x > \varepsilon$). Imposing decay at infinity yields

$$\widehat{g}_3(x,s|y) = A\,e^{-\kappa x}. \tag{E.21}$$

Region 2 ($0 < x < \varepsilon$). The general solution reads

$$\widehat{g}_2(x,s|y) = B\cosh(\kappa x) + C\sinh(\kappa x). \tag{E.22}$$

Region 1 ($-N < x < 0$). Due to the source term at $x = y \in (-N, 0)$, we solve piecewise:

$$\widehat{g}_1(x,s|y) = \begin{cases} \widehat{g}_1^{<}(x,s|y), & -N < x < y, \\ \widehat{g}_1^{>}(x,s|y), & y < x < 0. \end{cases} \tag{E.23}$$

Imposing the reflecting (Neumann) wall at $x = -N$ is conveniently achieved by using the coordinate $(x+N)$. We take

$$\widehat{g}_1^{<}(x,s|y) = P\cosh\big(\kappa(x+N)\big), \qquad -N < x < y, \tag{E.24}$$

$$\widehat{g}_1^{>}(x,s|y) = Q\cosh\big(\kappa(x+N)\big) + R\sinh\big(\kappa(x+N)\big), \qquad y < x < 0. \tag{E.25}$$

Indeed, $\partial_x \cosh(\kappa(x+N)) = \kappa\sinh(\kappa(x+N))$ vanishes at $x = -N$.

E.7 Jump conditions at the source point $x = y$

The Green's function properties imply:

1. continuity at $x = y$,
2. a jump in the derivative fixed by the delta source.

Explicitly,

$$\widehat{g_1^<}(y,s|y) = \widehat{g_1^>}(y,s|y), \tag{E.26}$$

$$\partial_x \widehat{g_1^>}(y,s|y) - \partial_x \widehat{g_1^<}(y,s|y) = -\frac{1}{D}. \tag{E.27}$$

E.8 Matching conditions in Laplace space

The matching conditions (E.13) and (E.14) apply identically to the Laplace transforms.

At $x = 0$. From (E.22) one has $\widehat{g}_2(0) = B$ and $\partial_x \widehat{g}_2(0) = \kappa C$. Evaluating (E.25) at $x = 0$ (i.e. $x + N = N$) yields

$$\widehat{g}_1(0^-) = Q\cosh(\kappa N) + R\sinh(\kappa N), \qquad \partial_x \widehat{g}_1(0^-) = \kappa\left[Q\sinh(\kappa N) + R\cosh(\kappa N)\right]. \tag{E.28}$$

Thus,

$$B = \alpha\left[Q\cosh(\kappa N) + R\sinh(\kappa N)\right], \qquad C = Q\sinh(\kappa N) + R\cosh(\kappa N). \tag{E.29}$$

At $x = \varepsilon$. Using (E.22) and (E.21),

$$\widehat{g}_2(\varepsilon) = B\cosh(\kappa\varepsilon) + C\sinh(\kappa\varepsilon), \qquad \partial_x \widehat{g}_2(\varepsilon) = \kappa\left[B\sinh(\kappa\varepsilon) + C\cosh(\kappa\varepsilon)\right], \tag{E.30}$$

$$\widehat{g}_3(\varepsilon) = Ae^{-\kappa\varepsilon}, \qquad \partial_x \widehat{g}_3(\varepsilon) = -\kappa A e^{-\kappa\varepsilon}. \tag{E.31}$$

The interface conditions (E.14) imply

$$Ae^{-\kappa\varepsilon} = \alpha^{-1}\left[B\cosh(\kappa\varepsilon) + C\sinh(\kappa\varepsilon)\right], \tag{E.32}$$

$$-\kappa A e^{-\kappa\varepsilon} = \kappa\left[B\sinh(\kappa\varepsilon) + C\cosh(\kappa\varepsilon)\right]. \tag{E.33}$$

Eliminating A yields the transfer relation

$$\frac{C}{B} = -\frac{\cosh(\kappa\varepsilon) + \alpha\sinh(\kappa\varepsilon)}{\sinh(\kappa\varepsilon) + \alpha\cosh(\kappa\varepsilon)}. \tag{E.34}$$

For completeness, A is obtained from (E.32):

$$A = e^{\kappa\varepsilon}\alpha^{-1}\left[B\cosh(\kappa\varepsilon) + C\sinh(\kappa\varepsilon)\right]. \tag{E.35}$$

E.9 Closed-form coefficients Q and R

To simplify notation, define

$$C_N := \cosh(\kappa N), \qquad S_N := \sinh(\kappa N), \qquad C_\varepsilon := \cosh(\kappa \varepsilon), \qquad S_\varepsilon := \sinh(\kappa \varepsilon), \tag{E.36}$$

and introduce

$$M := \frac{C_\varepsilon + \alpha S_\varepsilon}{S_\varepsilon + \alpha C_\varepsilon}. \tag{E.37}$$

Define further the combinations

$$\Xi := S_N + \alpha M C_N, \qquad \Lambda := C_N + \alpha M S_N. \tag{E.38}$$

Let $u := y + N \in (0, N)$ and denote

$$C_u := \cosh(\kappa u), \qquad S_u := \sinh(\kappa u). \tag{E.39}$$

Using the jump conditions (E.26)–(E.27) together with the interface transfer relation, one obtains explicitly

$$R = -\frac{C_u}{D\kappa}, \qquad Q = \frac{C_u}{D\kappa}\frac{\Lambda}{\Xi}. \tag{E.40}$$

Finally, from continuity at $x = y$ one finds

$$P = Q + R \tanh(\kappa u). \tag{E.41}$$

The remaining coefficients B, C, A are then given by (E.29) and (E.35).

E.10 Final Laplace-space Green's function

Let $v := x + N \in (0, N)$. The Laplace-transformed propagator is:

Region 1 ($-N < x < 0$).

$$\widehat{g}_1(x, s|y) = \begin{cases} P \cosh(\kappa v), & -N < x < y, \\ Q \cosh(\kappa v) + R \sinh(\kappa v), & y < x < 0, \end{cases} \tag{E.42}$$

with P, Q, R given in (E.40)–(E.41).

Region 2 ($0 < x < \varepsilon$).

$$\widehat{g}_2(x, s|y) = B \cosh(\kappa x) + C \sinh(\kappa x), \tag{E.43}$$

where

$$B = \alpha(QC_N + RS_N), \qquad C = QS_N + RC_N. \tag{E.44}$$

Region 3 ($x > \varepsilon$).

$$\widehat{g}_3(x,s|y) = A\, e^{-\kappa x}, \tag{E.45}$$

with A given by (E.35).

E.11 Return to $g_i(x,t|y)$

The time-domain propagators are obtained by inverse Laplace transformation:

$$g_i(x,t|y) = \mathscr{L}^{-1}[\widehat{g}_i(x,s|y)]\,(t), \qquad i = 1,2,3. \tag{E.46}$$

In particular, using the Bromwich inversion formula,

$$g_i(x,t|y) = \frac{1}{2\pi i}\int_{\gamma-i\infty}^{\gamma+i\infty} e^{st}\,\widehat{g}_i(x,s|y)\,ds, \qquad \gamma > 0. \tag{E.47}$$

Appendix F

Derivation of the Entropy Decomposition

In this appendix we derive explicitly the decomposition of the Shannon entropy of the particle position into a contribution from the region label and conditional spatial entropies as discussed in Section 4.5

F.1 Position distribution

Consider the probability density $g(x,t|y)$ of the particle position X at time t, given an initial position y. The spatial domain is partitioned into two disjoint regions

$$A = (-N, 0), \qquad B = (0, \infty),$$

so that

$$A \cap B = \varnothing, \qquad A \cup B = (-N, \infty).$$

The probability density can therefore be written piecewise as

$$g(x,t|y) = \begin{cases} g_A(x,t|y), & x \in A, \\ g_B(x,t|y), & x \in B. \end{cases}$$

The probabilities that the particle occupies the two regions are

$$p_A(y,t) = \int_A g_A(x,t|y)\,dx, \qquad p_B(y,t) = \int_B g_B(x,t|y)\,dx,$$

with

$$p_A(y,t) + p_B(y,t) = 1.$$

F.2 Conditional spatial densities

Within each region we introduce normalized conditional densities

$$\rho_A(x,t|y) = \frac{g_A(x,t|y)}{p_A(y,t)}, \qquad x \in A,$$

$$\rho_B(x,t|y) = \frac{g_B(x,t|y)}{p_B(y,t)}, \qquad x \in B.$$

By construction these densities satisfy the normalization conditions

$$\int_A \rho_A(x,t|y)\,dx = 1, \qquad \int_B \rho_B(x,t|y)\,dx = 1.$$

F.3 Entropy of the particle position

The Shannon differential entropy of the particle position is defined as

$$H(X) = -\int g(x,t|y)\log g(x,t|y)\,dx.$$

Since the spatial domain is the union of the two regions, the integral splits into two parts,

$$H(X) = -\int_A g_A(x,t|y)\log g_A(x,t|y)\,dx - \int_B g_B(x,t|y)\log g_B(x,t|y)\,dx.$$

F.4 Substitution of conditional densities

Using the definitions

$$g_A(x,t|y) = p_A\rho_A(x,t|y), \qquad g_B(x,t|y) = p_B\rho_B(x,t|y),$$

the entropy becomes

$$H(X) = -\int_A p_A\rho_A(x,t|y)\log\big[p_A\rho_A(x,t|y)\big]dx - \int_B p_B\rho_B(x,t|y)\log\big[p_B\rho_B(x,t|y)\big]dx.$$

Using the logarithmic identity

$$\log(ab) = \log a + \log b,$$

we obtain

$$H(X) = -\int_A p_A\rho_A(x)\big(\log p_A + \log\rho_A(x)\big)dx - \int_B p_B\rho_B(x)\big(\log p_B + \log\rho_B(x)\big)dx.$$

F.5 Separating the integrals

Expanding the integrals gives

$$H(X) = -\int_A p_A \rho_A(x) \log p_A \, dx - \int_A p_A \rho_A(x) \log \rho_A(x) \, dx$$

$$- \int_B p_B \rho_B(x) \log p_B \, dx - \int_B p_B \rho_B(x) \log \rho_B(x) \, dx.$$

The first and third terms contain constants inside the integrals, so they simplify using the normalization of the conditional densities. For example,

$$- \int_A p_A \rho_A(x) \log p_A \, dx = -p_A \log p_A \int_A \rho_A(x) \, dx = -p_A \log p_A.$$

Similarly,

$$- \int_B p_B \rho_B(x) \log p_B \, dx = -p_B \log p_B.$$

F.6 Identification of spatial entropies

The remaining terms can be written as

$$-p_A \int_A \rho_A(x) \log \rho_A(x) \, dx$$

and

$$-p_B \int_B \rho_B(x) \log \rho_B(x) \, dx.$$

We therefore define the conditional spatial entropies

$$H(\rho_A) = -\int_A \rho_A(x) \log \rho_A(x) \, dx,$$

$$H(\rho_B) = -\int_B \rho_B(x) \log \rho_B(x) \, dx.$$

Substituting these definitions yields

$$H(X) = -p_A \log p_A - p_B \log p_B + p_A H(\rho_A) + p_B H(\rho_B).$$

F.7 Final decomposition

Defining the entropy of the region label

$$H(R) = -p_A \log p_A - p_B \log p_B,$$

we obtain the decomposition

$$H(X) = H(R) + p_A H(\rho_A) + p_B H(\rho_B).$$

This expression shows that the total entropy of the particle position consists of two contributions: the entropy associated with the uncertainty of which region the particle occupies, and the conditional spatial entropy within each region.

Appendix G

Derivation of the Single-Particle Propagator

As discussed in Section 4.5, in this appendix we determine the single-particle propagator

$$g(q,u,t \mid q_0,u_0),$$

which enters the many-body construction. This is the Green's function of the ballistic transport equation in the presence of

- a perfectly reflecting wall at $q=-N$,
- a partially transmitting defect at $q=0$.

Throughout we assume $q_0 \in (-N,0)$.

G.1 Transport Equation

The propagator satisfies the Liouville equation

$$\partial_t g + u\,\partial_q g = 0,$$

with initial condition

$$g(q,u,0 \mid q_0,u_0) = \delta(q-q_0)\delta(u-u_0).$$

In the absence of boundaries the solution follows from characteristics:

$$g_{\text{free}}(q,u,t \mid q_0,u_0) = \delta(q-q_0-u_0t)\delta(u-u_0).$$

Thus motion is purely ballistic with constant velocity.

G.2 Boundary Rules

Reflecting wall at $q = -N$. At the wall elastic reflection occurs:

$$u \longrightarrow -u.$$

This boundary is deterministic and preserves probability.

Defect at $q = 0$. At the defect scattering is stochastic:

transmission with probability $T(u)$, reflection with probability $R(u) = 1 - T(u)$.

Reflection reverses the velocity,

$$u \to -u,$$

while transmission preserves it. Once transmitted into $q > 0$, the particle propagates freely and does not return.

G.3 Method of Images and Renewal Expansion

Let

$$v = u_0, \qquad \xi(t) = q_0 + vt.$$

Define the first defect hitting time t_d (if $v > 0$):

$$t_d = \frac{-q_0}{v},$$

and the round-trip time between defect and wall:

$$\tau = \frac{2N}{|v|}.$$

The successive defect encounter times are

$$t_s = t_d + s\tau, \qquad s = 0, 1, 2, \ldots$$

whenever defined.

For any fixed t, only finitely many t_s satisfy $t_s \leq t$. These times determine the admissible number of defect reflections.

G.4 Transmitted Sector ($q > 0$)

To reach $q > 0$ at time t, the particle must have transmitted once.

If transmission occurs after s defect reflections (at time t_s), the associated probability weight is

$$T(v)R(v)^s.$$

After transmission the motion is free into $q > 0$. Thus the transmitted contribution is

$$g_>(q,u,t \mid q_0,v) = \sum_{s=0}^{\infty} T(v)R(v)^s\,\delta\big(q-\xi(t)+2sN\big)\,\delta(u-v)\mathbf{1}_{t\geq t_s}.$$

The indicator function enforces causality: only those defect encounters that have occurred by time t contribute. Note that we didn't need it for the hydrodynamic case in point hard rods because we were evolving densities and not the green's function.

G.5 Reflected Sector ($q < 0$)

If no transmission has occurred by time t, the particle remains in $(-N,0)$. Suppose exactly s defect reflections have occurred. The associated probability weight is

$$R(v)^s.$$

The admissible time window for exactly s reflections is

$$t_s \leq t < t_{s+1}.$$

Using the image construction for the reflecting wall, the reflected sector splits according to the final velocity.

(i) Final velocity $u = v$ (even total reflections).

$$g_<^{(+)}(q,u,t) = \sum_{s=0}^{\infty} R(v)^s\mathbf{1}_{t_s\leq t<t_{s+1}}\Big[\delta\big(q-\xi(t)+2sN\big)+\delta\big(q+\xi(t)-2sN-2N\big)\Big]\,\delta(u-v).$$

(ii) Final velocity $u = -v$ (odd total reflections).

$$g_<^{(-)}(q,u,t) = \sum_{s=0}^{\infty} R(v)^{s+1}\mathbf{1}_{t_s\leq t<t_{s+1}}\,\delta\big(q+\xi(t)-2sN\big)\,\delta(u+v).$$

G.6 Full Green's Function

The exact propagator is

$$g(q,u,t \mid q_0,v) = g_>(q,u,t) + g_<^{(+)}(q,u,t) + g_<^{(-)}(q,u,t).$$

This construction:

- solves the Liouville equation away from the boundaries,
- satisfies elastic reflection at $q = -N$,
- implements stochastic scattering at $q = 0$,
- preserves total probability:

$$\int_{-N}^{\infty} dq \int du\, g(q,u,t \mid q_0,u_0) = 1.$$

G.7 Position Propagator

The position propagator entering the many-body construction is

$$\tilde{g}_i(q,t) = \int du\, g(q,u,t \mid q_{i0},u_{i0}).$$

Integrating over u yields

$$\tilde{g}_i(q,t) = \sum_{s=0}^{\infty} T(u_{i0}) R(u_{i0})^s \delta\big(q - q_{i0} - u_{i0}t + 2sN\big) \mathbf{1}_{t \geq t_s}$$

$$+ \sum_{s=0}^{\infty} R(u_{i0})^s \mathbf{1}_{t_s \leq t < t_{s+1}} \Big[\delta\big(q - q_{i0} - u_{i0}t + 2sN\big) + \delta\big(q + q_{i0} + u_{i0}t - 2sN - 2N\big) \Big]$$

$$+ \sum_{s=0}^{\infty} R(u_{i0})^{s+1} \mathbf{1}_{t_s \leq t < t_{s+1}} \delta\big(q + q_{i0} + u_{i0}t - 2sN\big).$$

For fixed t, only finitely many s contribute.

G.8 Independence from Rod Length

The propagator g depends only on single-particle ballistic dynamics and boundary scattering rules. It is independent of the rod length a.

The hard-core interaction enters the many-body problem only through the ordering constraint imposed by the hard-rod mapping.

Bibliography

[1] Anatoli Polkovnikov, Krishnendu Sengupta, Alessandro Silva, and Mukund Vengalattore. Colloquium: Nonequilibrium dynamics of closed interacting quantum systems. *Reviews of Modern Physics*, 83:863, 2011.

[2] Jens Eisert, Markus Friesdorf, and Christian Gogolin. Quantum many-body systems out of equilibrium. *Nature Physics*, 11:124–130, 2015.

[3] Pasquale Calabrese and John Cardy. Quantum quenches in extended systems. *Journal of Statistical Mechanics*, 2007.

[4] Luigi Amico, Rosario Fazio, Andreas Osterloh, and Vlatko Vedral. Entanglement in many-body systems. *Reviews of Modern Physics*, 80:517, 2008.

[5] J. Eisert, M. Cramer, and M. B. Plenio. Colloquium: Area laws for the entanglement entropy. *Reviews of Modern Physics*, 82(1):277–306, February 2010.

[6] Pasquale Calabrese and John Cardy. Evolution of entanglement entropy in one-dimensional systems. *Journal of Statistical Mechanics*, 2005.

[7] Nicolas Laflorencie. Quantum entanglement in condensed matter systems. *Physics Reports*, 646:1–59, 2016.

[8] Pasquale Calabrese and John Cardy. Entanglement entropy and quantum field theory. *Journal of Statistical Mechanics: Theory and Experiment*, (06):P06002, 2004.

[9] Madhumita Saha, Manas Kulkarni, and Abhishek Dhar. Generalized hydrodynamics description of the page curve-like dynamics of a freely expanding fermionic gas. *SciPost Physics*, 2024.

[10] Don N Page. Information in black hole radiation. *Physical Review Letters*, 71:3743, 1993.

[11] Don N. Page. Time dependence of hawking radiation entropy. *Journal of Cosmology and Astroparticle Physics*, 2013(09):028, 2013.

[12] J. M. Deutsch. Quantum statistical mechanics in a closed system. *Physical Review A*, 43(4):2046–2049, 1991.

[13] M. Srednicki. Chaos and quantum thermalization. *Physical Review E*, 50(2):888–901, 1994.

[14] Marcos Rigol, Vanja Dunjko, and Maxim Olshanii. Thermalization and its mechanism for generic isolated quantum systems. *Nature*, 452:854–858, 2008.

[15] Marcos Rigol, Vanja Dunjko, and Maxim Olshanii. Relaxation in a completely integrable many-body quantum system: An ab initio study of the dynamics of the highly excited states of 1d hard-core bosons. *Physical Review Letters*, 98(5):050405, 2007.

[16] Lev Vidmar and Marcos Rigol. Generalized gibbs ensemble in integrable lattice models. *Journal of Statistical Mechanics: Theory and Experiment*, (064007), 2016.

[17] Olalla A. Castro-Alvaredo, Benjamin Doyon, and Takato Yoshimura. Emergent hydrodynamics in integrable quantum systems out of equilibrium. *Physical Review X*, 6(4):041065, 2016.

[18] Bruno Bertini, Mario Collura, Jacopo De Nardis, and Maurizio Fagotti. Transport in out-of-equilibrium xxz chains: Exact profiles of charges and currents. *Physical Review Letters*, 117(20):207201, 2016.

[19] Vincenzo Alba and Pasquale Calabrese. Entanglement and thermodynamics after a quantum quench in integrable systems. *Proceedings of the National Academy of Sciences*, 114(30):7947–7951, July 2017.

[20] Vincenzo Alba and Pasquale Calabrese. Entanglement dynamics after quantum quenches in generic integrable systems. *SciPost Physics*, 4(3), March 2018.

[21] Elliott H. Lieb and Derek W. Robinson. The finite group velocity of quantum spin systems. *Communications in Mathematical Physics*, 28(3):251–257, 1972.

[22] C. Boldrighini, R. L. Dobrushin, and Y. M. Sukhov. One-dimensional hard rod caricature of hydrodynamics. *Journal of Statistical Physics*, 31:577–616, 1983.

[23] D. W. Jepsen. Dynamics of a simple many-body system of hard rods. *Journal of Mathematical Physics*, 6(3):405–413, 1965.

[24] Lewi Tonks. The complete equation of state of one, two and three-dimensional gases of hard elastic spheres. *Phys. Rev.*, 50:955–963, Nov 1936.

[25] Marko Ljubotina, Spyros Sotiriadis, and Tomaž Prosen. Non-equilibrium quantum transport in presence of a defect: the non-interacting case. *SciPost Phys.*, 6:004, 2019.

[26] Ingo Peschel and Viktor Eisler. Reduced density matrices and entanglement entropy in free lattice models. *Journal of Physics A: Mathematical and Theoretical*, 42(50):504003, 2009.

[27] C. N. Yang and C. P. Yang. Thermodynamics of a one-dimensional system of bosons with repulsive delta-function interaction. *Journal of Mathematical Physics*, 10(7):1115–1122, 1969.

[28] Herbert Spohn. *Large Scale Dynamics of Interacting Particles*. Texts and Monographs in Physics. Springer-Verlag, Berlin Heidelberg, 1991.

[29] Benjamin Doyon and Herbert Spohn. Dynamics of hard rods with initial domain wall state. *Journal of Statistical Mechanics: Theory and Experiment*, 2017(7):073210, July 2017.

[30] Jitendra Kethepalli, Andrew Urilyon, Tridib Sadhu, and Jacopo De Nardis. Ballistic macroscopic fluctuation theory via mapping to point particles. *SciPost Phys.*, 20:105, 2026.

[31] Claude E. Shannon. A mathematical theory of communication. *Bell System Technical Journal*, 27(3):379–423, 1948.

[32] Hannes Risken. *The Fokker-Planck Equation: Methods of Solution and Applications*. Springer-Verlag, Berlin, Heidelberg, 2nd edition, 1996.